

---

ETD Archive

---

2017

## **Influence Of Cross-Section Change During Directional Solidification On Dendrite Morphology, Macrosegregation And Defect Formation In Pb-6 wt Sb Alloy**

Claudine Lacdao  
*Cleveland State University*

Follow this and additional works at: <https://engagedscholarship.csuohio.edu/etdarchive>

 Part of the [Chemical Engineering Commons](#)

**How does access to this work benefit you? Let us know!**

---

### **Recommended Citation**

Lacdao, Claudine, "Influence Of Cross-Section Change During Directional Solidification On Dendrite Morphology, Macrosegregation And Defect Formation In Pb-6 wt Sb Alloy" (2017). *ETD Archive*. 959.  
<https://engagedscholarship.csuohio.edu/etdarchive/959>

This Thesis is brought to you for free and open access by EngagedScholarship@CSU. It has been accepted for inclusion in ETD Archive by an authorized administrator of EngagedScholarship@CSU. For more information, please contact [library.es@csuohio.edu](mailto:library.es@csuohio.edu).

INFLUENCE OF CROSS-SECTION CHANGE DURING  
DIRECTIONAL SOLIDIFICATION ON DENDRITE  
MORPHOLOGY, MACROSEGREGATION AND DEFECT  
FORMATION IN Pb-6 WT Sb ALLOY

CLAUDINE LACDAO

Bachelor of Science in Chemical Engineering

Cleveland State University

MAY 2016

Submitted in partial fulfillment of requirements for the degree

MASTER OF SCIENCE IN CHEMICAL ENGINEERING

at the

CLEVELAND STATE UNIVERSITY

AUGUST 2017

**We hereby approve this thesis  
for**

**Claudine C. Lacdao**

**Candidate for the Master of Science in Chemical Engineering degree for the  
Department of Chemical and Biomedical Engineering  
and CLEVELAND STATE UNIVERSITY's  
College of Graduate Studies**

---

Thesis Chairperson, Surendra Tewari, Ph.D.

Department of Chemical & Biomedical Engineering  
Department & Date

---

Thesis Committee Member, Orhan Talu, Ph.D.

Department of Chemical & Biomedical Engineering  
Department & Date

---

Thesis Committee Member, Christopher Wirth, Ph.D.

Department of Chemical & Biomedical Engineering  
Department & Date

---

Thesis Committee Member, Nolan B. Holland, Ph.D.

Department of Chemical & Biomedical Engineering  
Department & Date

Student's Date of Defense: August 18, 2017

## DEDICATION

This thesis is dedicated to my parents, Roberto and Judith Lacdao. Your unconditional love and support have always carried me throughout all my academic endeavors.

## ACKNOWLEDGEMENTS

First and foremost, I would like to thank God for His love and guidance throughout my life especially during my time at Cleveland State University and throughout this research experience. You have blessed me in countless ways with a caring research advisor, an incredible department, and a wonderful family. All glory is Yours!

I would like to thank my graduate advisor, Dr. Surendra Nath Tewari, for welcoming me to the Advanced Material Science research team and encouraging me to drive many tasks into completion. I am truly grateful for your understanding. Thank you for your support and consistent guidance throughout the research and particularly during the thesis composal period.

I would like to thank my committee members: Dr. Nolan Holland, Dr. Orhan Talu and Dr. Christopher Wirth for taking the time to read my manuscript and giving helpful critiques while maintaining a flexible schedule. I thank Dr. Masoud Ghods, for his permission to include a portion of his dissertation research results as part of my thesis. Thank you also for assisting me and attempting to answer the endless brigade of questions I had in my time in the lab.

In addition, I would like to go back to my roots and thank Ms. Jo'anne Lewis, who introduced me to physics and engineering in St. Croix Educational Complex High School at a young age. Your spirit of adventure in regard to research and excitement in regard to teaching has continuously inspired me over the years.

Speaking of roots, I would like to thank my family who patiently encouraged me throughout this long and arduous process. Many thanks to my grandmother, Rosario Campos and Aunt Mary Jane Padilla for all the wisdom they have imparted to me over the years. I would also like to acknowledge all my friends for their unconditional support.

Finally I would like to thank the Microgravity Materials Research Program at NASA – Marshall Space Flight Center for their continued support of this research.

**INFLUENCE OF CROSS-SECTION CHANGE DURING DIRECTIONAL  
SOLIDIFICATION ON DENDRITE MORPHOLOGY, MACROSEGREGATION  
AND DEFECT FORMATION IN Pb-6 %Sb ALLOY**

**CLAUDINE LACDAO**

**ABSTRACT**

The purpose of this research is to examine the dendrite array morphology, macrosegregation, and defect formation caused by the fluid flow at the abrupt cross-section changes during directional solidification of Pb-6% Sb alloy. Four 24-cm long cylindrical alloy samples were directionally solidified in graphite crucibles: two having a constant diameter (9-mm) grown at 10.4 and 63.1  $\mu\text{m s}^{-1}$ , one having an abrupt cross-section decrease (from 12.7 to 6.35 mm) and one having an abrupt increase (from 6.35 to 12.7 mm) by pulling down the alloy containing cylindrical graphite crucibles from the upper hot-zone of a stationary vertical furnace into its cold-zone below. Microstructures were examined on transverse slices cut along the length of the directionally solidified samples. Dendrite spacing and distribution were characterized on these transverse sections. The Pb-6% Sb alloy was selected as a low melting point analog for commercially used multicomponent nickel-base superalloys, because its thermophysical properties are well characterized. Also, a density inversion occurs in the inter-dendritic melt in the “mushy-zone” during directional solidification of this alloy, because the density of the melt decreases as Sb content increases from the array tips at the top of the mushy zone to the eutectic at their bottom. In constant cross-section crucibles, the formation of dendrite-trees in the mushy

zone will be subject only to this “plume type” convection as solidification proceeds from the bottom end of the crucible to its top. Whereas in crucibles with abrupt cross-section change, the solidifying mushy-zone will be subject to additional “cross-section change induced” solidification shrinkage flow, when the speed of the liquid flowing downwards to feed the solidification shrinkage occurring below, will either suddenly accelerate or decelerate, because of the abrupt area change. This sudden change in the incoming fluid speed may break slender side-branches of dendrite trees. These broken dendrite fragments may rotate, sink, and grow further to develop into misaligned “spurious” grains. The “plume type of flow” is different than the “steeppling convection flow” which was recently examined during directional solidification of Al-19% Cu and Al-7% Si alloys by Dr. Masoud Ghods in our laboratory.



# TABLE OF CONTENTS

	Page
ABSTRACT.....	vi
LIST OF FIGURES .....	xii
LIST OF TABLES .....	xv
CHAPTER .....	1
I. GENERAL INTRODUCTION.....	1
1.1. Alloy Industrial Applications and Solidification .....	1
1.1.1. Single Crystal Turbine Blades .....	1
1.1.2. Conventional Casting.....	2
1.1.3. Directional Solidification.....	3
1.2. Mushy Zone Morphology .....	3
1.2.1. Dendrites.....	4
1.2.2. Eutectic .....	5
1.3. Thermosolutal Convection During Directional Solidification .....	6
1.3.1. Solutally Stable and Thermally Stable Interdendritic Melt Configuration.....	6
1.3.2. Solutally Unstable and Thermally Stable Interdendritic Melt Configuration.....	8
1.4. Relevant Works.....	10
1.4.1. Convection in Pb-Sb Binary Alloy System .....	10
1.4.2. Theoretical Models .....	11

1.4.2.1.	Primary Dendrite Nearest Neighbor Spacing Model.....	12
1.4.2.2.	Primary Dendrite Trunk Diameter Model.....	14
1.5.	Pb-Sb Binary Alloy Melt Characteristics .....	14
1.6.	Experimental Goals.....	15
II.	EXPERIMENTAL AND ANALYTICAL PROCEDURES .....	18
2.1.	Bridgeman Furnace Apparatus .....	18
2.2.	Graphite Crucible and Pb-6% Sb Sample Assembly .....	19
2.3.	Directional Solidification.....	20
2.4.	Specimen Preparation and Metallography .....	21
2.4.1.	Longitudinal Samples .....	21
2.4.2.	Transverse Samples .....	21
2.4.3.	Cutting, Mounting, And Polishing.....	22
2.4.4.	Microscopy .....	23
2.5.	Image Analysis.....	24
2.5.1.	Image Stitching .....	24
2.5.2.	Primary Dendrite Trunk Diameter And Dendrite Trunk Centers.....	25
2.5.3.	Nearest Neighbor Spacing .....	27
2.5.4.	Fraction Eutectic .....	28
III.	RESULTS AND DISCUSSION .....	32
3.1.	Effects of Growth Speed on Solutally Unstable Pb-6wt% Sb with Constant Cross Section.....	32

3.1.1.	Transverse Macrostructure Images .....	32
3.1.2.	Longitudinal Macrosegregation Dependence on Growth Speed and Fraction Solidified.....	34
3.1.3.	Primary Dendrite Trunk Diameter Dependence on Growth Speed and Distance From the Base .....	36
3.1.4.	Nearest Neighbor Spacing Dependence on Growth Speed and Distance From the Base.....	37
3.2.	Effects of Cross-section Contraction in Pb-6 % Sb (Solutally Unstable) vs. Al-19 % Cu (Solutally Stable) Systems .....	39
3.2.1.	Longitudinal and Transverse Macrostructure Images.....	39
3.2.2.	Comparison of Longitudinal Macrosegregation in Pb-6% Sb vs. Al-19% Cu Directionally Solidified with Cross-section Contraction.....	42
3.2.3.	Comparison of Primary Dendrite Trunk Diameter in Pb-6% Sb vs. Al-19% Cu Directionally Solidified with Cross-section Contraction.....	44
3.2.4.	Comparison of Nearest Neighbor Spacing in Pb- 6% Sb vs. Al-19% Cu Directionally Solidified with Cross- section Contraction .....	46
3.3.	Effects of Cross-Section Expansion in Pb-6% Sb (Solutally Unstable) vs. Al-19% Cu (Solutally Stable) Systems.....	47

3.3.1. Longitudinal and Transverse Macrostructure	
Images.....	47
3.3.2. Longitudinal Chemical Inhomogeneity .....	49
3.3.3. Primary Dendrite Trunk Diameter.....	51
IV. CONCLUDING REMARKS.....	55
V. RECOMMENDATIONS FOR FUTURE RESEARCH.....	58
REFERENCES .....	59
APPENDIX A.....	64
APPENDIX B .....	69
APPENDIX C .....	72
APPENDIX D.....	79
APPENDIX E .....	82

## LIST OF FIGURES

Figure 1 Sketch representing columnar to equiaxed grain transition in a traditional cast. <sup>6</sup>	3
Figure 2 Succinonitrile – 9 wt. % Water “Transparent alloy” directionally solidified ( $\sim 5\mu\text{m s}^{-1}$ , $\sim 30\text{Kcm}^{-1}$ ) (Dr. Grugel, NASA-MSFC) <sup>8</sup>	5
Figure 3 (a) Schematic Temperature, Concentration and Density Profiles in interdendritic Liquid, Al-Cu <sup>8</sup> (b) Image of transverse slice of an Al-19 % Cu alloy, grown at $10\mu\text{m s}^{-1}$ . This depicts an example of transverse phase macrosegregation.	8
Figure 4 (a) Schematic Temperature, Concentration and Density Profiles in interdendritic Liquid, Pb-Sb <sup>8</sup> (b) Image of transverse slice of an Pb-6 % Sb alloy, grown at $10.4\mu\text{m s}^{-1}$ . This depicts an example of channel formation as because of plume type thermos-solutal convection.	9
Figure 5 Schematic Convection Profiles in Directionally solidified Pb-Sb systems under (a) cross section contraction and (b) expansion.	10
Figure 6 Pb-Sb Phase Diagram <sup>20</sup>	15
Figure 7 Images of Bridgman-technique furnace assembly for directional solidification <sup>8</sup>	19
Figure 8 Image of typical graphite crucible used for solidification	20
Figure 9 Temperature versus distance for thermocouples TC1, TC2, TC3, and TC4 for sample Pb-Sb-3.	21
Figure 10 Screen captures of bounding rectangle measurement for trunk diameter	27
Figure 11 Typical example depicting the thresholding procedure of an 8-bit image of an Pb-Sb transverse slice with corresponding intensity histograms.	29

Figure 12 Typical example depicting the watershed and particle area cut-off procedure of a binary image.....	30
Figure 13 Transverse macrostructure of Pb-6Sb 9 cm from base grown at (a) 10.4 $\mu\text{m/s}$ (b) 63.1 $\mu\text{m/s}$ .....	33
Figure 14 Longitudinal macrosegregation ( $C_s/C_o$ ) as a function of fraction solidified ( $f_s$ ) for Pb-6Sb grown at (a) 10.4 $\mu\text{m/s}$ (b) 63.1 $\mu\text{m/s}$ and corresponding $\log(C_s/C_o)$ as a function of $\log(1-f_s)$ for Pb-6Sb grown at (a) 10.4 $\mu\text{m/s}$ (b) 63.1 $\mu\text{m/s}$ .....	35
Figure 15 Average primary dendrite trunk diameter as a function of location for Pb-6Sb grown at (a) 10.4 $\mu\text{m/s}$ (b) 63.1 $\mu\text{m/s}$ .....	37
Figure 16 Nearest neighbor spacing as a function of location for Pb-6Sb grown at (a) 10.4 $\mu\text{m/s}$ (b) 63.1 $\mu\text{m/s}$ .....	39
Figure 17 Longitudinal macrostructure of Pb-6Sb grown at 11.5 $\mu\text{m/s}$ with cross section contraction. (Diameter decrease from 12.7 mm to 6.35 mm).....	40
Figure 18 Transverse macrostructure of (a) Pb-6Sb grown and (b) Al-19Cu <sup>11</sup> at 11.5 $\mu\text{m/s}$ with cross section contraction. ....	41
Figure 19 Longitudinal macrosegregation (% Solute) as a function of distance from contraction for (a) Pb-6 Sb and (b) Al-19Cu <sup>11</sup> .....	43
Figure 20 Average primary dendrite trunk diameter as a function of distance from contraction for (a) Pb-6Sb and (b) Al-19Cu <sup>11</sup> .....	45
Figure 21 Nearest neighbor spacing as a function of distance from contraction for (a) Pb-6Sb and (b) Al-19Cu <sup>11</sup> .....	47
Figure 22 Longitudinal macrostructure of Pb-6Sb grown at 8.7 $\mu\text{m/s}$ with cross section expansion. (Diameter increase from 6.35 mm to 12.7 mm) .....	48

Figure 23 Transverse macrostructure of (a) Pb-6Sb grown at 8.7 $\mu\text{m/s}$ and (b) Al-19Cu <sup>11</sup> at 10 $\mu\text{m/s}$ with cross section expansion.....	49
Figure 24 Longitudinal macrosegregation (%Solute) as a function of distance from expansion for (a) Pb-6 Sb and (b) Al-19Cu <sup>11</sup> .....	51
Figure 25 Primary dendrite trunk diameter as a function of distance from expansion for (a) Pb-6 Sb and (b) Al-19Cu <sup>11</sup> .....	53
Figure 26 Nearest neighbor spacing as a function of distance from expansion for (a) Pb-6 Sb and (b) Al-19Cu <sup>11</sup> .....	54

## LIST OF TABLES

Table I Select thermophysical properties of Pb – 6 wt. pct. Sb System, used in theoretical models to predict primary dendrite spacing. <sup>27</sup> .....	13
Table II Growth speeds applied to Pb – 6 wt. pct. Sb samples.....	20
Table III Polishing procedure for 9-mm and 12.7-mm diameter sections sample preparation.....	23
Table IV Polishing procedure for 6.35-mm diameter sections sample preparation.....	23



## **CHAPTER I**

### **GENERAL INTRODUCTION**

#### **1.1. Alloy Industrial Applications and Solidification**

##### **1.1.1. Single Crystal Turbine Blades**

Bridgman directional solidification technology is widely used to fabricate the first stage turbine blades used in the modern gas-turbine engines for applications in both the aircraft engines and terrestrial power generating engines.<sup>1,2</sup> These first stage turbine blades are the most critical component in advanced gas turbine engines, as these are the most stressed high-temperature components of a gas-turbine engine.<sup>3</sup> Multicomponent nickel-based superalloys having a mono crystal dendrites oriented parallel to [100] direction along the blade length, are fabricated by directional solidification (DS) using ceramic investment casting shell molds. Because the [100] orientation provides the blade its maximum stress-rupture and thermal fatigue life, presence of any spurious (not aligned along [100]) grains is highly detrimental to its mechanical properties and must be avoided during directional solidification.<sup>4,5</sup> These blades have a complex geometrical shape, involving cross-section

increase and decrease at the blade-root and often a cross-section increase at the blade-tip locations. In addition, they also have complex internal cooling channels which are formed by directional solidification of the melt through many cross-section changes. Two techniques are used to achieve the [100] orientation. The first technique uses a [100] single crystal seed kept at the shell bottom, which is re-melted and fused with the rest of the melt before directional solidification of the blade. The other technique uses a small diameter helix shaped constriction at the shell bottom to help select one near [100] orientation grain from many incoming randomly oriented grains from below, which are generated when the hot melt, poured through the shell touches a quench block kept at the shell bottom.<sup>4</sup> A presence of “misoriented” spurious grains in the blade casting is a major cause of rejection during the process. It is believed that shrinkage-driven (thermal volumetric contraction) and thermosolutal convection associated with solidification through cross-section changes are responsible for the formation of spurious grains at these cross-section change locations.<sup>4</sup>

### **1.1.2. Conventional Casting**

In metalworking, conventional alloy casting refers to a process in which hot liquid metal melt is poured into a cold mold that contains a hollow cavity of the desired geometry to allow for the metal solidification. Component composition and mold geometry dictate heat transfer, thermal gradients, and solidification speeds. As shown schematically in Figure-1, solidification begins when the hot melt comes in contact with the cold mold forming many equiaxed grains. Competition among nucleation sites influences the growth of these grains. Grains oriented more favorably to the heat extraction direction grow at the expense of the unfavorably oriented ones resulting in a columnar grain morphology. The

rest of the melt continues to cool as solidification proceeds. If the melt undercools below its liquidus temperature, new randomly oriented grains of solid nucleate and grow yielding the equiaxed grain morphology during the final phase of solidification in the casting interior (Figure-1).

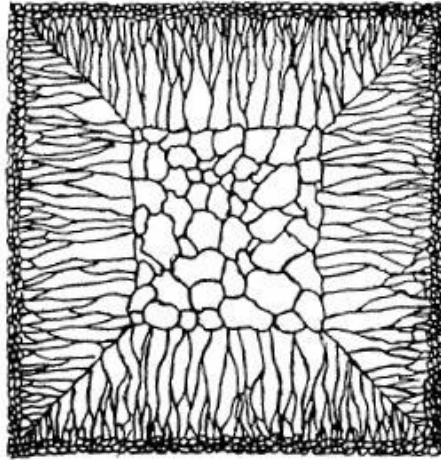


Figure 1 Sketch representing columnar to equiaxed grain transition in a traditional cast.<sup>6</sup>

### **1.1.3. Directional Solidification**

Directional solidification imposes a relatively constant thermal gradient in a single direction to maintain a single liquid-solid interface. Heat is extracted in only one direction by maintaining adiabatic walls on all sides except one. During solidification, the alloy containing ampoule is moved away from the heat source at a desired ‘growth’ rate  $R$  [cm/s] while maintaining an imposed thermal gradient  $G$  [K/cm] at the liquid-solid interface. For a high thermal gradient to growth rate ratio in a binary alloy, the liquid-solid interface has a planar liquid-solid front morphology. However, for most other cases the alloys are grown at a low thermal gradient to growth rate ratio where DS results in the formation of a two-phase (liquid+solid) mushy zone between the all liquid region at the hot end above, and the all-solid region at the cold end the mold below.<sup>7</sup>

### **1.2. Mushy Zone Morphology**

### 1.2.1. Dendrites

The mushy-zone, shown in Figure-2 for a transparent organic alloy (Succinonitrile – 9 wt. % Water) typically consists of arrays of “tree” like features, called primary dendrites. The trunk diameter of these primary dendrite trees increases from their tips in the vicinity of the all-liquid region above to the eutectic temperature at the bottom below which all solid-region exists. These trees in Face Centered Cubic (FCC) alloys have orthogonal side-branches (secondary arms), the side-branches have their own orthogonal branches (tertiary arms) and so-on. The four-fold orthogonal symmetry of the side-branching in FCC is associated with the requirement that the solid phase growing along the [100] direction surround itself with the lowest liquid-solid surface energy planes, which are (111) for the FCC crystals. The primary dendrite spacing, primary dendrite trunk diameter, secondary and tertiary branch spacing are all dependent on growth conditions and the alloy physical properties. Faster growth speeds produce finer features and tighter packing, and therefore smaller grains.<sup>7</sup> Morphology and distribution of primary dendrites, secondary dendrites and tertiary dendrites depend upon the local alloy composition and local solidification conditions, and they all determine the mechanical properties of the solidified components. Therefore, any inhomogeneity in the microstructure is disconcerting.

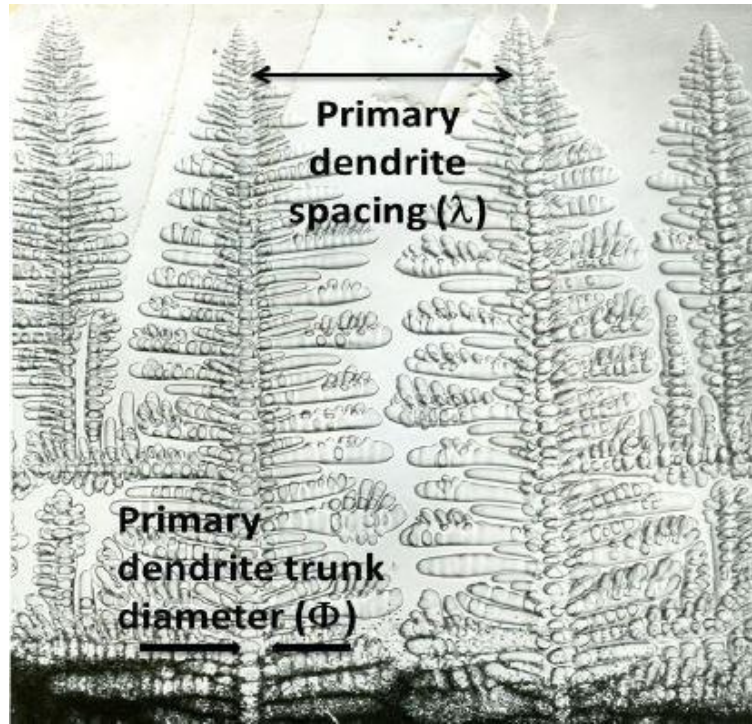


Figure 2 Succinonitrile – 9 wt. % Water “Transparent alloy” directionally solidified ( $\sim 5\mu\text{m s}^{-1}$ ,  $\sim 30\text{Kcm}^{-1}$ ) (Dr. Grugel, NASA-MSFC)<sup>8</sup>

### 1.2.2. Eutectic

As shown schematically in Figure-3(a) in binary alloys the primary dendrite tips begin to form from the surrounding liquid as the temperature falls below the alloy liquidus temperature ( $T_l$ ). Because of the curvature undercooling the primary dendrite tip temperature ( $T_t$ ) is, however, slightly below  $T_l$ . Therefore, in alloys where the solute partition coefficient ( $k$ ) (ratio of the solute content of the solid phase and that of the liquid in equilibrium) is less than one, the composition of the liquid at the array tips ( $C_t$ ) is slightly above the nominal solute content of the alloy,  $C_0$ . Since the diffusion coefficient of solute in solid is at least two orders of magnitude slower than that in the liquid, further solidification of the primary dendrites results in continued solute enrichment of the interdendritic melt, because of the solute continually being rejected from the growing solid and getting accumulated in the interdendritic melt. The interdendritic melt ultimately

reaches the eutectic composition at the base of the dendrite arrays and the two-phase eutectic solid forms there. The interdendritic melt is, therefore, solute poor near the array tips and solute rich at the base of dendrite array. Depending upon whether the increasing solute results in increased melt density, such as in Al-19 % Cu alloy, or it results in reduced melt density as is the case with the Pb-6 % Sb alloy the density of the interdendritic melt in the mushy-zone either increases downwards or decreases downwards during directional solidification with melt on the top and the solid below. Natural convection driven by gravity can occur when the less dense melt is below and the higher density melt above. Since the temperature gradient alone (higher temperature less dense melt on top of the lower density cooler melt below) is stabilizing during directional solidification, convection in the mushy zone should solely depend upon the solutal effects alone.

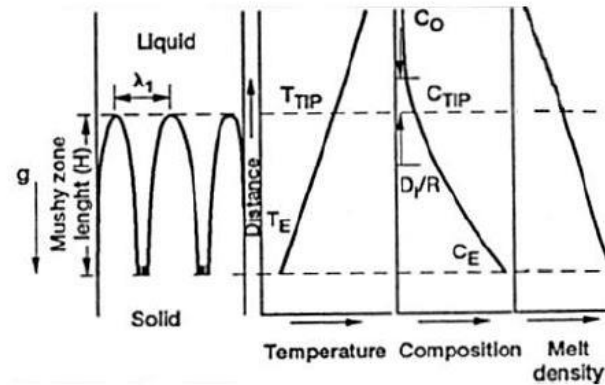
### **1.3. Thermosolutal Convection During Directional Solidification**

#### **1.3.1. Solutally Stable and Thermally Stable Interdendritic Melt Configuration**

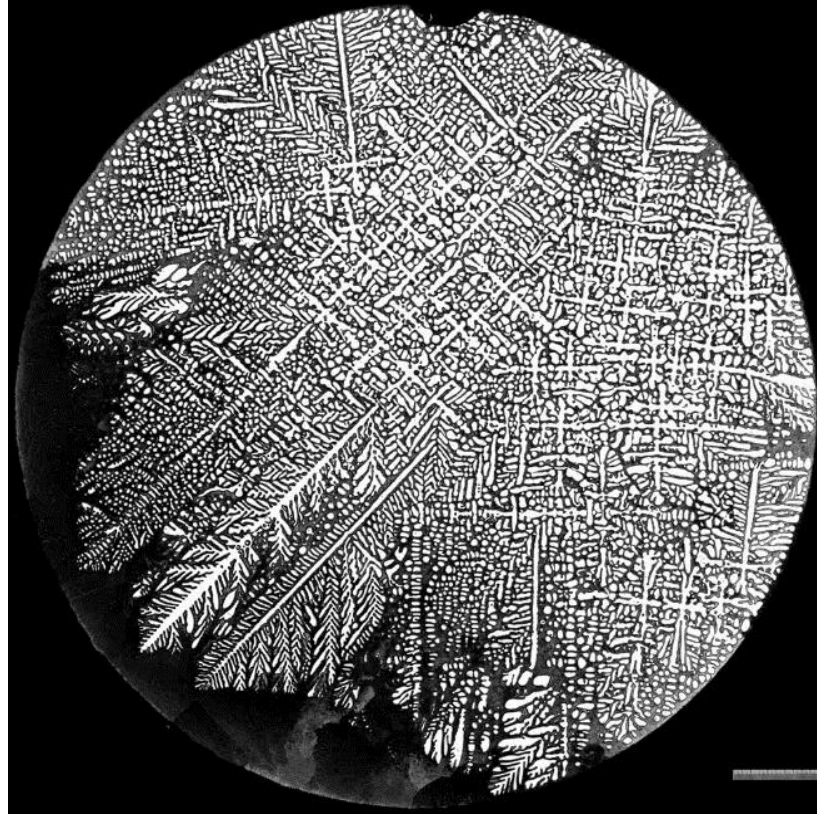
The interdendritic concentration gradient in alloys where solute-rich liquid is densest at the dendrite roots ( $C_o < C_{tip} < C_E$ ) stabilizes natural convection as seen on Figure-3(a) as is the case for Al-Cu systems (Aluminum: 2.70 g/cm<sup>3</sup> and Copper: 8.98 g/cm<sup>3</sup> at melting temperature).<sup>7</sup> Therefore no convection is expected in the mushy-zone. The liquid alloy, in and above the mushy zone, in an upward directional solidification setup, is also thermally stable against natural convection because of earth's gravitational vector (g).

However, small radial thermal gradient or any misalignment of the crucible with respect to gravity vector can initiate natural convection via a “steeping type” of convection. The “steeping convection” occurs when the solute rich ( $C_i$ ) heavier density melt ahead of the leading dendrite in an array begins to flow radially downwards towards

the tips of its lagging neighbors and stifles their growth further. This results in a mushy-zone which does not have a uniform mushy-zone length through-out. The primary dendrites get clustered (“steepled”) in the leading regions and the solute content radially outwards can sometimes reach the eutectic composition,  $C_E$ . This results in extensive radial chemical inhomogeneity (macrosegregation) and also microstructural inhomogeneity as shown in Figure-3(b) for a Al-19% Cu alloy solidified at  $10 \mu\text{m s}^{-1}$  growth speed.



(a)



(b)

Figure 3 (a) Schematic Temperature, Concentration and Density Profiles in interdendritic Liquid, Al-Cu<sup>8</sup>  
 (b) Image of transverse slice of an Al-19 % Cu alloy, grown at  $10 \mu\text{m s}^{-1}$ <sup>7</sup>. This depicts an example of transverse phase macrosegregation.

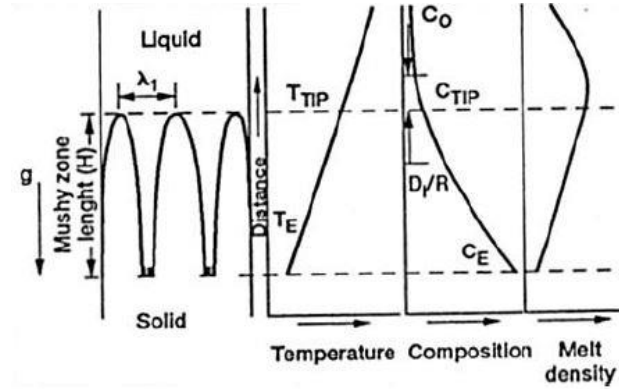
### 1.3.2. Solutally Unstable and Thermally Stable Interdendritic Melt

#### Configuration

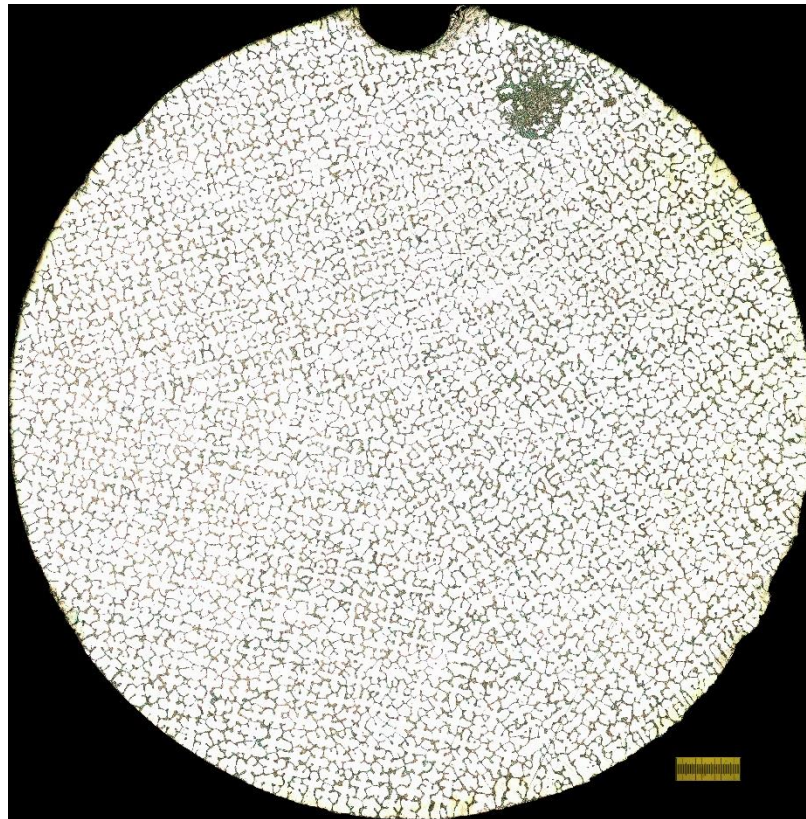
Directional solidification of Pb-6% Sb alloy on the other hand is expected to result in a thermally stable, but solutally unstable interdendritic melt configuration as is shown in Figure - 4(a). Despite the stabilizing thermal profile a density inversion occurs when the solute-rich melt near the dendrite roots is less dense than that near the dendrite tip (Lead:  $11.34 \text{ g/cm}^3$  to Antimony:  $6.68 \text{ g/cm}^3$  at melting temperature). This convection called “plume type” convection leads to compositional inhomogeneities along the solidified length of the sample (longitudinal macrosegregation),<sup>9,10</sup> and also results in



microstructural inhomogeneities on the sample cross-section (as shown in Figure - 4(b)). A highly segregated channel-segregate can clearly be seen in this transverse microstructure of a Pb-6% Sb alloy directionally solidified at  $10.4 \mu\text{m s}^{-1}$ .



(a)



(b)

Figure 4 (a) Schematic Temperature, Concentration and Density Profiles in interdendritic Liquid, Pb-Sb<sup>8</sup>  
 (b) Image of transverse slice of an Pb-6 % Sb alloy, grown at  $10.4 \mu\text{m s}^{-1}$ . This depicts an example of channel formation as because of plume type thermos-solutal convection.

## 1.4. Relevant Works

### 1.4.1. Convection in Pb-Sb Binary Alloy System

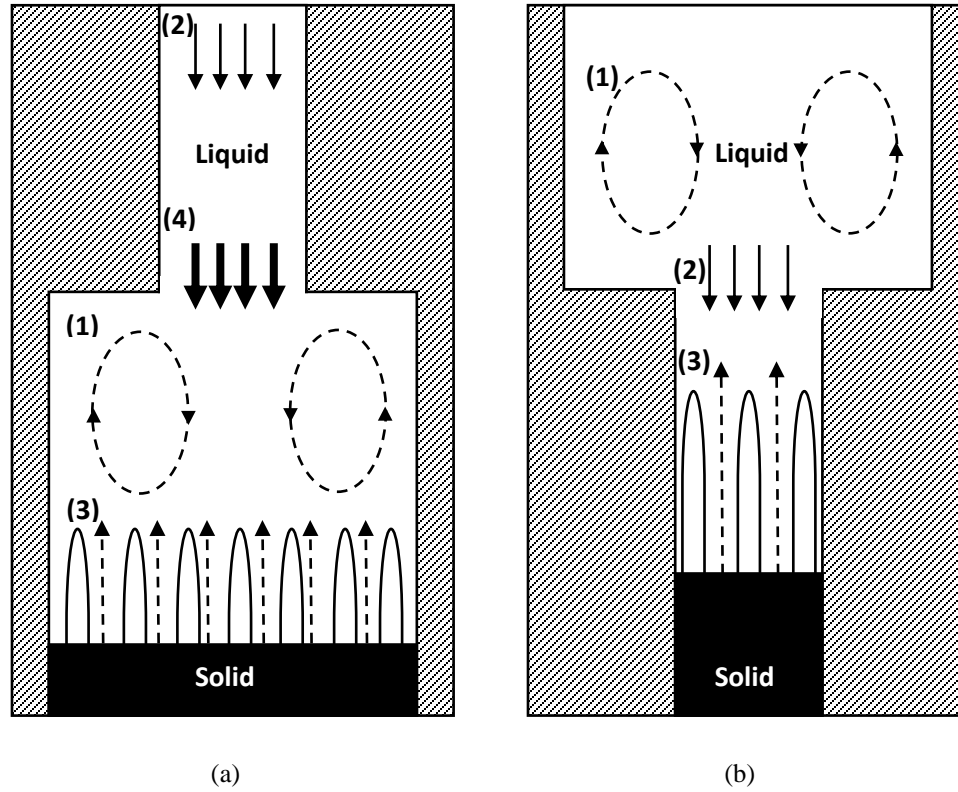


Figure 5 Schematic Convection Profiles in Directionally solidified Pb-Sb systems under (a) cross section contraction and (b) expansion.

Figure - 5 (a) and (b) are schematic representations of the expected interactions between three types of potential convective fluid flows and the mushy-zone during directional solidification of Pb-6% Sb alloy in a graphite mold containing abrupt changes in cross-sections; (1) thermal convection indicated by circular dotted-line flows caused by radial thermal gradients, (2) “solidification-shrinkage” convection indicated by the vertical down-wards arrows, and (3) thermosolutal convection indicated by vertical upwards arrows with dotted lines.

The two-fold increase in the thermal diffusivity of the solid metal forming from the liquid causes an inward heat flow from the graphite mold creating a radial thermal gradient

in the melt.<sup>6</sup> This initiates “thermal convection” cells where the liquid flows upwards close to the mold walls and downwards at the center as depicted in Figure - 5 (a.1) and (b.1). This also causes the isotherms to become convex toward the all-liquid region above the mushy-zone.<sup>11</sup>

Shrinkage convection occurs due to the significantly high thermal expansion coefficient of the liquid melt ( $\beta_T$ ) compared to the solid. A solidifying liquid shrinks in volume as it solidifies (solid is less dense than liquid) therefore the liquid rushes downwards to maintain continuity. There is a constant shrinkage convection pushing the fluid downwards even in the constant cross-section region of the mold. However, its magnitude increases when the solid forming in the larger cross-section below begins to reach the abrupt cross-section reduction region, because the smaller cross-section liquid column has to now feed the larger cross-section solidifying below (Figure - 5(a)). In a cross section expansion situation as seen on Figure - 5(b), the magnitude of the shrinkage flow decreases as compared with the larger cross-section portion of the mold above because a smaller cross-section solidifying below is being fed by a larger cross-section area melt pool above.

There is also the convection that occurs because of the temperature and concentration gradient within the interdendritic melt discussed in the previous section. The density of the melt is lower at the base of the dendrite, this generates a “plume” type of flow where the liquid flows upwards against the gravity vector. This flow can bring solute rich liquid upwards faster than the local isotherm growth speeds which can cause localized remelting and fragmentation of the slender side-branches already formed there.<sup>12</sup>

#### **1.4.2. Theoretical Models**

#### 1.4.2.1. Primary Dendrite Nearest Neighbor Spacing Model

Analytical or numerical modeling for mushy-zone dendritic array morphology formation during directional solidification involves consideration of multiple parameters. Microstructure characteristics such as primary dendrite spacing, the dendrite tip-radius, and tip composition have been analytically and numerically modeled after making many simplifying assumptions.<sup>13,14</sup> Some of these assumptions include pure thermal and solutal diffusion (no convection) and simple “needle” (unbranched) shaped primary dendrites. Numerical models have been used to simulate convection through a mushy-zone of dendrites<sup>1,15,16</sup>, but several simplifications were made to solve for the moving liquid-solid interface. The primary challenge for numerical simulation has been the “non-linear” nature of the phenomenon. Convective contribution to the heat and solute transport in the melt, mush, and the solid has only been calculated for a “time invariant liquid-solid mushy-zone structure” (for example known and constant permeability), but the “mushy-zone” dendritic array morphology (for example permeability) is changed by the presence of “convection”.<sup>6</sup>

Despite these limitations, several semi-theoretical models have been proposed to predict some of the macro morphology parameters such as dendrite tip radius ( $\rho$ ), dendrite tip composition ( $C_{tip}$ ), and primary spacing of dendrite trunks ( $\lambda$ ). Some popular models in literature include Kurz-Fisher<sup>13</sup>, Trivedi<sup>17</sup> and Hunt-Lu<sup>14,18</sup>. The Hunt-Lu model is a semi-empirical model that uses experimental polynomial ‘fit’ parameters and has proven to correlate well over a wide range of growth speeds, thermal gradients, and compositions. This will be the only model used to compare experimental results for primary spacing. The Hunt-Lu model [HL] is a function of the dimensionless parameters:

$$G' = \frac{G\Gamma}{(mC_0)^2}$$

$$V' = \frac{V\Gamma}{DmC_o}$$

$$\lambda' = \frac{\lambda m C_o}{\Gamma}$$

$$\text{where } \Delta T_o = \frac{m_L C_o (k-1)}{k}$$

G is the effective thermal gradient,  $\Gamma$  is the capillary length (proportional to the ratio of solid-fluid surface energy to the heat of fusion), D is the diffusion coefficient, k is the solute partition coefficient,  $C_o$  is the initial alloy composition, mL is the liquidus slope, and  $\lambda$  is the trunk diameter. For calculation, all variables are assumed to be constant. The following is the HL model with parameters:

- Curvature Undercooling  $\Delta T'_\sigma$

$$\Delta T'_\sigma = 0.41(V' - G')^{0.51}$$

- Tip radius  $\rho$

$$\rho = \frac{2\Gamma}{\Delta T'_\sigma \Delta T_o}$$

- Primary spacing  $\lambda'$

$$\lambda' = 0.15596V'^{(a-0.75)}(V' - G')^{0.75}G'^{-0.6028}$$

$$a = -1.131 - 0.1555 \log(G') - 0.007589[\log(G')]^2$$

As referenced for the Pb-6 %Sb system in Table I,  $k=0.31$ ,  $D=5 \times 10^{-5} \text{ cm}^2\text{s}^{-1}$ ,  $\Gamma=0.12 \text{ }\mu\text{mK}^{-1}$ ,  $m=6.62 \text{ K/wt.pct.}$  and  $C_o=7 \text{ wt. pct.}$

Table V Select thermophysical properties of Pb – 6 wt. pct. Sb System, used in theoretical models to predict primary dendrite spacing.<sup>27</sup>

Name	Variable	Units	Value
Liquid Temperature	TL	°C	288.1
Liquid Slope	mL	K/wt%	-6.78
Solute Partition Coefficient	k	Dimensionless	0.31

Eutectic Temperature	TE	°C	252.5
Heat of Fusion	$\Delta h_f$	Jm <sup>-3</sup>	$2.79 \times 10^8$
Eutectic Composition	CE	wt%	11.2
Gibbs-Thomson Coefficient	$\Gamma$	$\mu\text{mK}$	0.105

#### 1.4.2.2. Primary Dendrite Trunk Diameter Model

The primary dendrite trunk diameter is a useful metric that correlates well with the actual solidification processing parameters and complements the conventionally used primary, secondary, and tertiary arm spacings. A model developed by Tewari et. al <sup>19</sup> was used to calculate the predicted value for primary trunk diameter in this study.

$$\phi^3 = 96 \frac{D_l \Gamma}{VG(1-k)} \ln \left\{ \frac{1 + \frac{VGt}{m_l C_0}}{1 + \frac{VGt_0}{m_l C_0}} \right\} + \phi_0^3 \quad \text{Equation 1}$$

Where  $\phi_0 = 6.59r_t$  is the initial trunk diameter with  $r_t$  being the dendrite tip radius,  $D_l$  is the solute diffusion coefficient in the liquid,  $V$  is growth speed,  $G$  is thermal gradient,  $\Gamma$  is Gibbs-Thompson coefficient,  $k$  is solute partition coefficient,  $m_l$  is liquidus slope and  $C_0$  is the alloy composition.

### 1.5. Pb-Sb Binary Alloy Melt Characteristics

Solute enrichment during binary alloy solidification changes the melt density. In a Pb-Sb alloy system, the solute (antimony) has a significantly lower density than the solvent (lead) (6.684 g/cm<sup>3</sup> and 11.34 g/cm<sup>3</sup> respectively at melting point). A density inversion occurs in the interdendritic melt in the “mushy-zone” during directional solidification, because the density of the melt decreases as Sb content increases from the array tips at the

top of the mushy zone to the eutectic at the bottom. This unique phenomenon that leads to various macrosegregation was one of the reasons why Pb-6 % Sb was selected for this study. A Pb-Sb phase diagram is shown in Figure - 6 along with tabulated thermophysical properties required by theoretical models to calculate primary dendrite spacing listed in Table I.

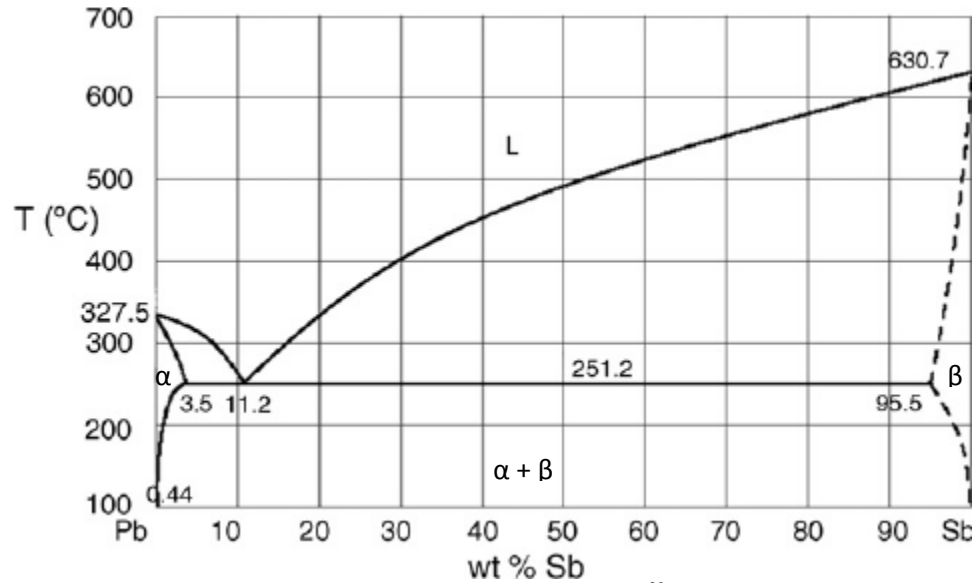


Figure 6 Pb-Sb Phase Diagram<sup>20</sup>

Liquid temperature is the melting temperature, liquid slope is the slope of the liquidus line on the phase diagram, solute partition coefficient is the ratio of compositions for the two phases at a given temperature, eutectic temperature is the temperature at which eutectic phase forms, eutectic composition is the overall composition of the eutectic phase, Gibbs-Thomson coefficient is a constant describing the surface curvature effects for phase equilibrium, and the solutal capillary length is the characteristic length defined by the surface tension between the two phases.

## 1.6. Experimental Goals

Macrosegregation caused by a cross-section change attributed to the changes in thermally induced flow was previously examined and modeled for Al-4.5 % Cu.<sup>9,10,21</sup>

Multiple studies have indicated that convection is the primary cause of irregular mushy-zone morphology that was observed as decrease in primary spacing, secondary spacing, and misoriented grain formation.<sup>22-28</sup> In Pb-Sb systems density inversion induces additional convection in the interdendritic region. There are limited experimental studies which examine both the macrosegregation and the microstructural changes caused by convection associated with cross-section change during directional solidification in Pb-Sb systems. The purpose of this study is to examine the mushy-zone morphology and composition change associated with cross-section change during directional solidification of Pb – 6 wt. pct. Sb alloys at varying directional solidification growth speeds. The lead-antimony alloy was selected in-order to consider the mushy zone convection caused by melt density inversion (solutal-driven convection) and to observe the role of “cross-section change” driven convection during directional solidification. This project has four specific purposes:

1. Carry out directional solidification of Pb-6% Sb alloy through constant cross-section at two growth speeds: 10.4 and 63.1  $\mu\text{m s}^{-1}$ .
2. Carry out directional solidification of Pb-6% Sb alloy through cross-section increase and cross-section decrease at low growth speed.
2. Measure mushy-zone morphology (primary dendrite spacing, primary dendrite trunk diameter) along the length of directionally solidified samples by using image-analysis techniques and establish trends if any.
3. Establish image analysis techniques for a quantitative analysis of phase amounts distribution in the microstructure as an indicator of macrosegregation.
4. Measure transverse and longitudinal macrosegregation associated with cross-section change during directional solidification and establish trends if any.



This data is expected to help identify solidification processing parameters for future low gravity experiments on the International Space Station.

## **CHAPTER II**

### **EXPERIMENTAL AND ANALYTICAL PROCEDURES**

#### **2.1. Bridgeman Furnace Apparatus**

Directional solidification was conducted using the apparatus set up shown in Figure - 7. The assembly consists of a cylindrical quartz chamber attached to two stainless steel flanges for the top and bottom support. To maintain good vacuum during solidification a diffusion pump vacuum was used to keep the chamber at  $\sim 2 \times 10^{-4}$  torr. A sixty watt RF power supply is used to create the hot-zone of the Bridgeman furnace assembly. Temperature along the length of the crucible is recorded by a data logger from four thermocouples. The cylindrical hollow graphite susceptor is enclosed within a 28 cm long insulating alumina shell. To minimize heat loss above the cylinder a 0.5 cm insulating shell is kept at the top portion of the susceptor and a 2 cm long insulating ceramic hollow disk was placed at the bottom of the susceptor. Two tantalum wires tied to the top stainless steel flange kept the furnace assembly within the alumina shell. The lead shell and the induction heating coils that make up the RF generator can be seen from a zoomed in image on the right in Figure - 7. The graphite crucible containing the Pb-6% Sb alloy cylinders (will be

discussed in great detail later) is inserted into the hanging furnace from the bottom for alloy re-melting and its subsequent directional solidification. The alloy containing crucible is attached to a stainless-steel feed through rod at the bottom. The sample is kept within the graphite crucible as it is withdrawn from the furnace to cool the water cooled inner walls of the graphite enclosure. Flowing water within the two-walled assembly of the chamber allows the inner wall to be kept at room temperature. A DC motor coupled to a worm gear arrangement is used for the sample translation. Vertical translation allows the graphite crucible to be pulled out or inserted into the Bridgman furnace.



Figure 7 Images of Bridgman-technique furnace assembly for directional solidification <sup>8</sup>

## **2.2. Graphite Crucible and Pb-6% Sb Sample Assembly**

The feed rods used in these experiments were prepared using lead and antimony of highest purity. Figure - 8 below shows a typical graphite crucible used for these experiments. From the cold end of the crucible, a 9 mm diameter by 2.8 mm long Pb-6 %

Sb alloy seed is inserted with known [100] crystal orientation. To fuse feed melt with the [100] oriented Pb-6 % Sb alloy seed kept at the bottom, the cast feed rods inserted from the top of the crucible are melted during heating. It is important to take extra caution to ensure only partial melting of the [100] seed at the bottom.



Figure 8 Image of typical graphite crucible used for solidification

### 2.3. Directional Solidification

The graphite crucible set up is inserted into the vacuum chamber and attached to the stainless steel feed through a rod passing through the bottom flange. The mechanical and diffusion pump is then used to evacuate the quartz chamber and apply a  $2 \times 10^{-4}$  torr vacuum. The cooling water valves are opened and RF generator turned on. A steady-state hot zone temperature of about  $750^{\circ}\text{C}$  is achieved by heating the graphite crucible at a preset temperature. It is then inserted into the furnace and TC1 through TC4 temperatures are continuously recorded. The feed rod is re-melted and fused with the seed aligned at the bottom. The sample is withdrawn from the furnace at the desired growth speed. Table II list the growth speeds for four of the directionally solidified specimens.

Table VI Growth speeds applied to Pb – 6 wt. pct. Sb samples

Sample ID	Sample Dimension	Growth Speed
Pb-Sb-12-24	Constant 9 mm	$10.4 \mu\text{m/s}$
Pb-Sb-12-22	Constant 9 mm	$63.1 \mu\text{m/s}$
Pb-Sb-3	12.7 - 6.35 mm	$11.5 \mu\text{m/s}$
Pb-Sb-1	6.35 - 12.7 mm	$8.7 \mu\text{m/s}$

Thermocouple ID# TC1, TC2, TC3, and TC4 temperature profiles recorded during directional solidification of sample Pb-Sb-3 are shown in Figure - 9 as an example of a

typical temperature profile during directional solidification. The temperature versus time data has been transformed to temperature versus distance data using the known sample translation speed, in this case, 11.5  $\mu\text{m/s}$  for Pb-Sb-3.

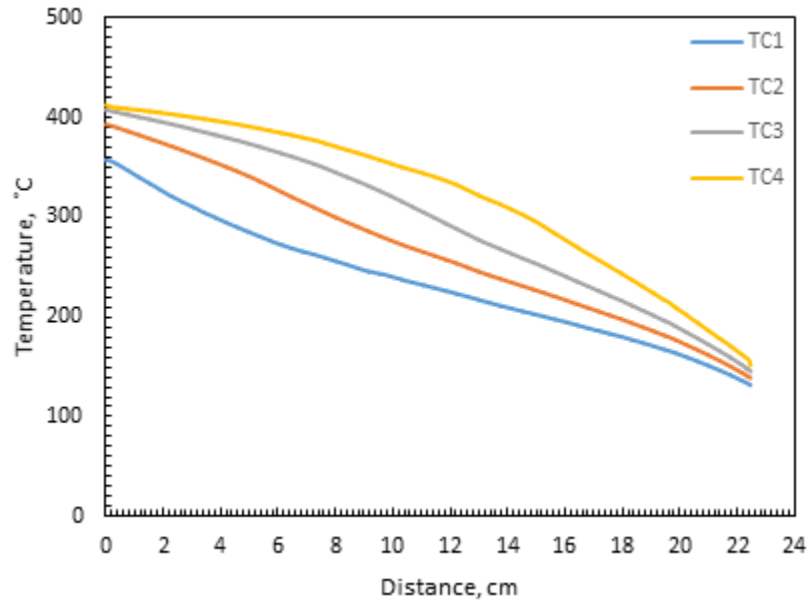


Figure 9 Temperature versus distance for thermocouples TC1, TC2, TC3, and TC4 for sample Pb-Sb-3.

## 2.4. Specimen Preparation and Metallography

### 2.4.1. Longitudinal Samples

The crucible was removed from the furnace after complete cooling. It is then prepared for cutting and mounting. Approximately 9 mm long portion, starting from about -3.5 mm below the neck of contracting cross-section to +5.5 mm. Approximately 5.1 mm long portion was cut for the longitudinal image of the experiment under abrupt expansion, starting from about -0.7 mm below the neck of the expansion +4.4 mm above.

### 2.4.2. Transverse Samples

Transverse images along the length were taken to examine morphology features such as trunk diameter, nearest neighbor spacing, and fraction eutectic. To distinguish the

correct orientation, each slice was marked which side was “hot”, closest to the aforementioned “hot-zone” during solidification). Each was then mounted, polished, and imaged for data extraction and analysis. Sample IDs with the corresponding location in the samples are shown in Tables V - VIII in the appendix of this report.

### **2.4.3. Cutting, Mounting, And Polishing**

A low-speed, variable RPM, precision wafer saw was used to cut the samples at various pre-determined locations shown in Tables V-VIII from the appendix. Diamond tipped low-grit precision saw blades of diameter 102 mm diameter by 0.3 mm thick were used. Between 25 - 50 grams of weight was added to the cutting arm, and blades were continuously wetted with cutting oil. Once sliced, the specimen’s “hot side” was marked and then smooth with a 9 mm Buehler Chemomet polishing cloth.

The specimens were then cold mounted. A cylindrical plastic mold was lubricated with industrial oil and the specimen was placed in the middle of the mold with the “hot side” facing downward. In a separate container, 30 mL of Struers Epofix resin was carefully mixed with 15 mL of Struers Epofix hardener to create an epoxy mixture. The epoxy mixture was then poured over the cylindrical mold and allowed to cure overnight. A Leica SM2500E Ultramiller was then used to further prepare the surface of the mounted sample for polishing and incident light investigation. The surface preparation procedure consists of two different steps: a preparation step carried out with a pre-miller and a finishing step during which a mirror-like surface is obtained. Any remainder particulates on the surface of the sample were cleaned and eliminated by using an ultrasonic bath.

An automatic wet abrasive grinder was used to ground and polish the samples. A 9 mm Buehler Chemomet polishing cloth was used in the final polishing stage. Chemomet

cloth is soft, porous, chemical-resistant, synthetic pad for softer materials which works well with the Pb-Sb surface. There are two layers of polishing grade, speed, force and time that was applied to the specimens listed on Table III and IV below.

*Table VII Polishing procedure for 9-mm and 12.7-mm diameter sections sample preparation*

Average Grade (Grit)	Downward Force/Sample	Time (min)	Polishing Pad RPM
9 mm Chemomet	5 lbs	6	110
9 mm Chemomet	5 lbs	6	110 (opposite rotational direction)

*Table VIII Polishing procedure for 6.35-mm diameter sections sample preparation*

Average Grade (Grit)	Downward Force/Sample	Time (min)	Polishing Pad RPM
9 mm Chemomet	3 lbs	4	110
9 mm Chemomet	3 lbs	2	110 (opposite rotational direction)
9 mm Chemomet	3 lbs	2	110

To eliminate contamination during polishing 0.05  $\mu\text{m}$  alumina slurry suspension was generously added to the surface of the polishing cloth. It is imperative to thoroughly clean the polishing cloth and specimens under running water after each round of polishing to eliminate alumina residue. Samples often need to be re-polished, solvated with ethyl alcohol, or cleaned in an ultrasonic bath to remove remaining colloidal alumina particles and oil. Avoid over-polishing as this can lead to wearing away of the softer alpha phase, creating an embossed surface with beveled edges on the final image that will be captured. Once finished, each sample was dried and then observed under the microscope for image capturing.

#### **2.4.4. Microscopy**

A metallurgical brightfield inverted Nikon microscope, 5.0-megapixel digital camera attachment and SPOT 5.0 Image software were used to capture magnified images of the sample's surface. Images were recorded at 5 times magnification for all specimens

for uniformity. For such a large field of view, several overlapping images were manually staged. At larger magnifications, 12.7 mm (1/2 in) diameter cross-sections required upwards of 120 images to cover the field of view. Original digital images were saved with .TIF extensions at the highest quality. Parameters such as light exposure, gamma corrections, gain, and color-filters were manually selected sample-to-sample to create best image quality. Ideal image quality was seen to possess constant light intensity across the whole field of view, for one phase and between samples and images. High contrast light absorption differences between lead and antimony also aid in distinguishing phases that were present. It was important to clean and align the microscope's projection lenses to capture consistent images. Typical settings include 140 ms of exposure, a 1.00 gain factor, gamma correction of 0.50, and a green-tint light filter. For each sample, a known 1 mm scale was imaged to record pixel to millimeter ratio for images. Oxide layers were known to grow rapidly on the metal's surface if samples were stored for later microscopy. This is often avoided to eliminate unevenness in the overall quality of the image.

## **2.5. Image Analysis**

### **2.5.1. Image Stitching**

Image stitching is the process of multiple photographic images with overlapping fields of view to produce a segmented high-resolution image by calibrating optical aberrations, and blending where applicable. Transformations for microscopic images are not required to adjust distortions. "Image registration" of locations or the process of transforming different sets of data into one coordinate system is significantly simplified by image stitching. Difficulties in conducting image stitching stem from intensity differences between images, intensity gradient in an image and partial unfocused features. Two images



can be blended by averaging intensities and colors to hide seams. Larger digital files require more computing capabilities, and therefore more difficult to stitch. Image stitching is a bottleneck procedure due to these potential complications. Note that the complexity of stitching will lead to computation errors, which leads to errors in image analysis. Adobe Photoshop CS5.1 on 64-bit Windows 7 on an HP z210 workstation was used to stitch the images in this study. A 120 image stitch, such as that for the larger cross-section area slices required 10 - 14 hours of computing time, and often lead to computer ‘freezes.’ A smaller 10 - 20 image collection for smaller cross-section area slices typically required 10 - 15 minutes to stitch.

Before analyzing the images for data subsequent slices are aligned to ensure that all have a similar reference point for rotation and centered within a background. Images were aligned using the original vertical cuts created for reference as microscopy requires manual alignment at a high magnification, and would, therefore, be more tedious. For the whole transverse end caps, dendrite feature’s orientation were measured between images, and then rotated to match.

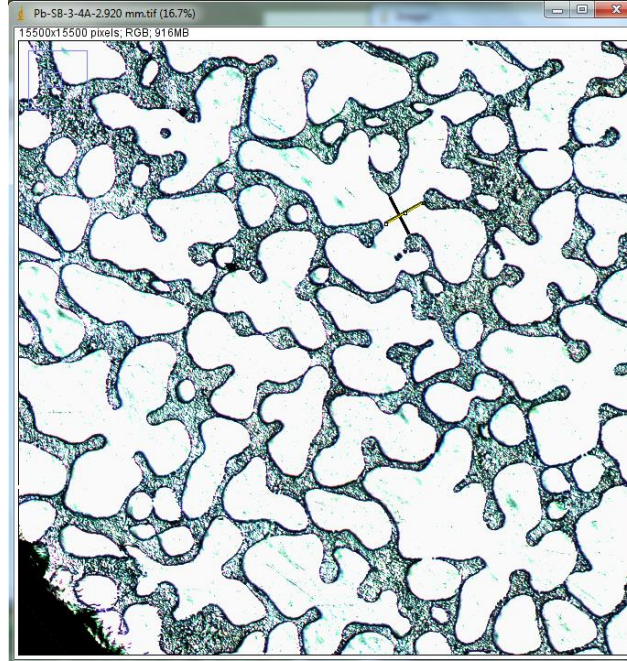
### **2.5.2. Primary Dendrite Trunk Diameter And Dendrite Trunk Centers**

An image processing program called ImageJ v. 1.46 was used to measure primary dendrite trunk diameter. ImageJ is an open source image analysis program that can be downloaded from <http://rsb.info.nih.gov/ij/> for a variety of operating systems. Drawing a line between two pixels with (x,y) coordinates can calculate length where  $d = \sqrt{x^2 + y^2}$ . Appropriate measurement values must be selected prior to drawing line segments. This is be done by choosing Analyze > Set Measurements > Bounding rectangle > OK, which measures a rectangle bounded by the two end points of the line segment acting as a

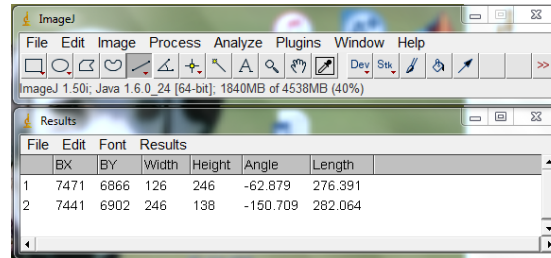
diagonal. After choosing the line-selection tool and making a line-selection on an image, choose Analyze > Measure will print a set of numbers for a 'Bounding rectangle.'

A bounding rectangle has 6 measurements labeled BX, BY, Width, Height, Angle, and Length. A rectangle can be drawn with the extreme values of x and y for the four corners of the rectangle provided a line segment with two sets of (x,y) coordinates. The line drawn is arbitrarily set as one of the diagonals. 'BX' and 'BY' are the upper-left x and y coordinate in pixels in relation to the upper-left corner of an image, 'Width' and 'Height' are the width and height of the bounding rectangle, 'Angle' is the minimum angle between the drawn line and an imaginary line facing due right from the 'starting' point for the drawn line, and 'Length' is the length of the drawn line.

For a dendrite trunk diameter measurement, two lines are drawn such that each line is a *minimum* distance spanning the trunk, as shown in Figure - 10. For an ideal well-formed dendrite, these two lines will be perpendicular to each other. The diameter of that trunk was taken as the average of those two lines lengths in pixels. Dendrite center was also calculated from these measurements by knowing the intersection of these two lines. This calculation was done through a computer program written in VBA coding language for Excel 2010, listed in the appendix. Though dendrite center absolute (x,y) coordinates are irrelevant, coordinates are important for spacing calculations which will be discussed in the later sections.



(a)



(b)

Figure 10 (a) A typical RGB image and (b) screen captures of bounding rectangle measurement for trunk diameter

### 2.5.3. Nearest Neighbor Spacing

Numerical analysis using (x,y) coordinates measured in ImageJ allows for the calculation of nearest neighbor spacing. The minimum of the set of all possible distances was calculated with a caveat that the set of all possible distances will not contain duplicates through the symmetric property of equality.<sup>8</sup> Given a set of (x,y) coordinates, a VBA macro code for Excel 2010 was written to calculate nearest neighbor spacing. This code is included in the appendix for reference.

## **2.5.4. Fraction Eutectic**

### **2.5.4.1. Thresholding**

The composition at a particular location can be calculated if the fraction eutectic is known. Fraction eutectic can be calculated using the area covered by the eutectic region divided by the total area of the sample. The difference in color intensities of the lead-rich and antimony-rich region based on their light absorption allows for identification of distinct structures from captured images. High-intensity lead-rich  $\alpha$  phase can then be separated from the antimony-rich eutectic. Thresholding allows for the separation of pixels based on intensity values. For an 8-bit image, pixels are labeled between 0 and 255 based on intensity where black is assigned a value of 0 and white is 255. A number is chosen where all numbers equaling that value or higher will be given a value of 255 and all lower a value of 0. Thresholding transforms an 8-bit grayscale image into a binary image of black and white pixels. Picking a proper cut-off intensity value is vital for accuracy to ensure user bias is not introduced as image intensity varies from sample to sample. ImageJ has a built-in thresholding algorithm under “default” which was used for thresholding.

A “Region of Interest” must always be selected before thresholding to eliminate unwanted background pixels that will not be included in the later calculation. In the ImageJ menu select: Edit > Selection > “Create Selection.” To execute the algorithm select: Image > Adjust > “Threshold.” The image can be inverted so that the dendrite phase is black and the antimony-rich phase is white. In the case where the values for black and white are inverted select: Image > Lookup Tables > “Invert LUT”. Hover over the black and white regions to ensure that the assigned values correspond to the correct color.

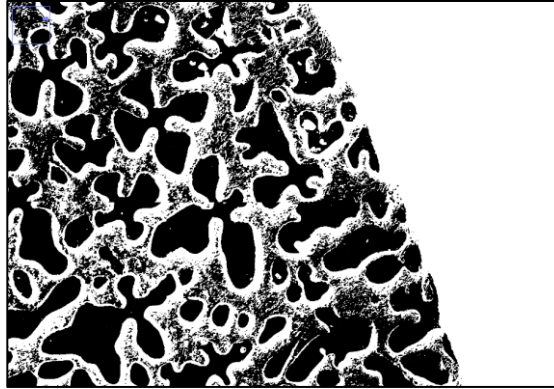


Figure 11 Typical example depicting the thresholding procedure of an 8-bit image of an Pb-Sb transverse slice with corresponding intensity histograms.

#### 2.5.4.2. Watershed

The eutectic phase is composed of both antimony-rich (white region) and lead-rich phase (black regions within eutectic). Since not all black pixels can be considered a fraction of the dendrites as seen from Figure - 11, the lead-rich metastable phases remaining within the eutectic which are colored similarly to the  $\alpha$  phase should be separated and eliminated prior to fraction eutectic calculation. A watershed algorithm was used to accomplish this.

A watershed transformation draws 1 pixel wide white pixels through geographical minimum distances between regions of white. Within the binary image, the antimony-rich white particles embedded into the lead-rich black landscape are connected by a spider web of lines, sectioning the lead-rich black landscape into particles. It should be noted that the drawn white pixels add to the white count and subtract from the black count by 0.5 - 1% of the total pixel count (which can be calculated by [black particle count before watershed] - [black particle count after watershed]).



Figure 12 Typical example depicting the watershed and particle area cut-off procedure of a binary image.

#### 2.5.4.3. Particle Size Cut-Off

After watershedding the image, individual particles are created from the previously connected lead-rich black regions within the eutectic. To eliminate eutectic  $\alpha$  phase from being included in the calculation of primary dendrite  $\alpha$  phase, particles having areas smaller than a specified pixel area cutoff value were ignored while measuring the area fraction occupied by primary dendrites. Pixel area cutoff value ranges from 1000-2500 pixels and may vary from image to image. Different cutoff values will affect results by 1-2% for 100% increase or decrease in area cutoff. Once this value is determined, the eutectic  $\alpha$  phase particles can be selected as a “Region of Interest” and are then filled with white to eliminate its fraction contribution.

#### 2.5.4.4. Fraction Eutectic Calculation

Fraction eutectic can be calculated once the eutectic black particles (eutectic  $\alpha$ ) are eliminated and a binary image has been created. Given a ‘Region of Interest’, the mean intensity value can be calculated. Particle’s values are 255 for white or 0 for black.

Therefore,  $[\text{mean intensity}]/255 = [\text{fraction alpha}]$  and  $1-[\text{fraction dendrite}] = [\text{fraction eutectic}]$ . Then from the lever rule,  $C_o^* = f_e * (C_B^\alpha - C_B^\beta) + C_B^\beta$ , where  $C_o^*$  is the local average composition, and  $f_e$  is fraction eutectic. As this process is standard from image to image, a macro was written for ImageJ to process a batch of images.

## **CHAPTER III**

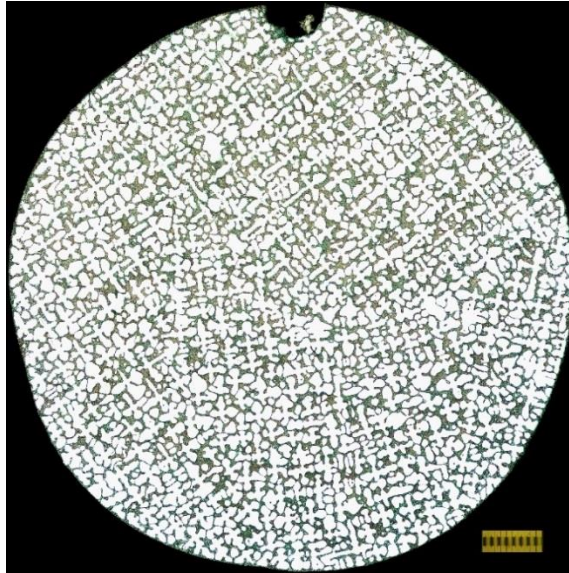
### **RESULTS AND DISCUSSION**

#### **3.1. Effects of Growth Speed on Solutally Unstable Pb-6wt% Sb with Constant Cross Section**

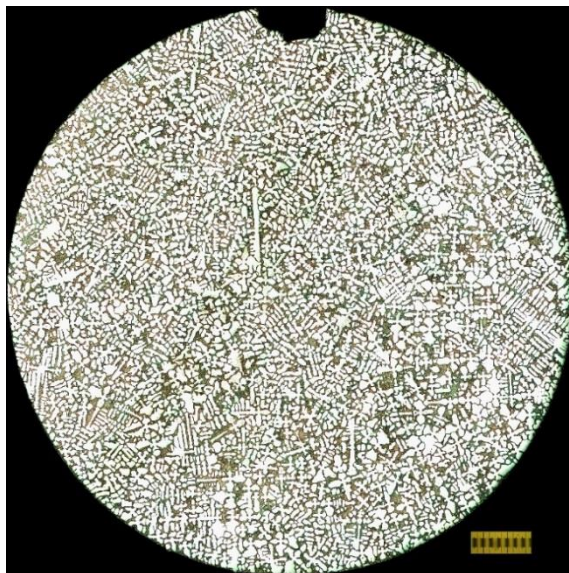
##### **3.1.1. Transverse Macrostructure Images**

Sample transverse images for Pb-6 % Sb grown at 10.4 and 63.1  $\mu\text{m/s}$  growth speeds are shown in Figure - 13 (a) and (b) below. The orthogonal bright features are representative of the solute-poor primary  $\alpha$  phase dendrites. The darker gray area is representative of the eutectic region comprising of both  $\alpha$  and  $\beta$  fine solid phases.





(a)



(b)

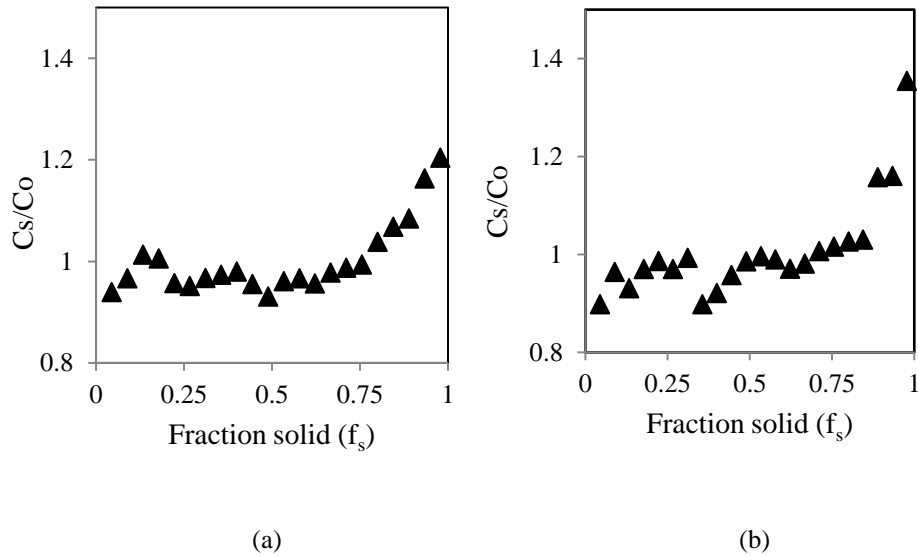
Figure 13 Transverse macrostructure of Pb-6Sb 9 cm from base grown at (a) 10.4  $\mu\text{m/s}$  (b) 63.1  $\mu\text{m/s}$

The dark looking, eutectic-concentrated regions present in the transverse images signify macrosegregation from channel formation. This means that in some regions the upper composition and permeability range with respect to the material properties (which can be further characterized by the Lewis and Prandtl numbers that were not calculated in

this study) allowed channels to become diffuse and convection to become general and essentially turbulent.<sup>29</sup> In addition, the transverse images suggest that increasing growth speed decreases trunk diameter. From visual observations increasing growth speed also seem to decrease the primary dendrite spacing. Trends in longitudinal chemical inhomogeneity, trunk diameter and primary dendrite spacing involved further image and quantitative analysis which is discussed in the sections that follow.

### 3.1.2. Longitudinal Macrosegregation Dependence on Growth Speed and Fraction Solidified

The average composition values after solidification at various locations were calculated from fraction eutectic data obtained from transverse images at each corresponding locations and the equation  $C_s = -3.351 * (f_E)^2 + 13.48 * f_E + 0.802$  relating  $f_E$  to the average solute content  $C_s$ .<sup>7</sup> Figure - 14 (a) and (b) illustrates the relationship between the ratios of the average composition to the nominal composition as fraction solid increases for specimens with constant cross section grown at 10.4 and 63.1  $\mu\text{m/s}$ , respectively.



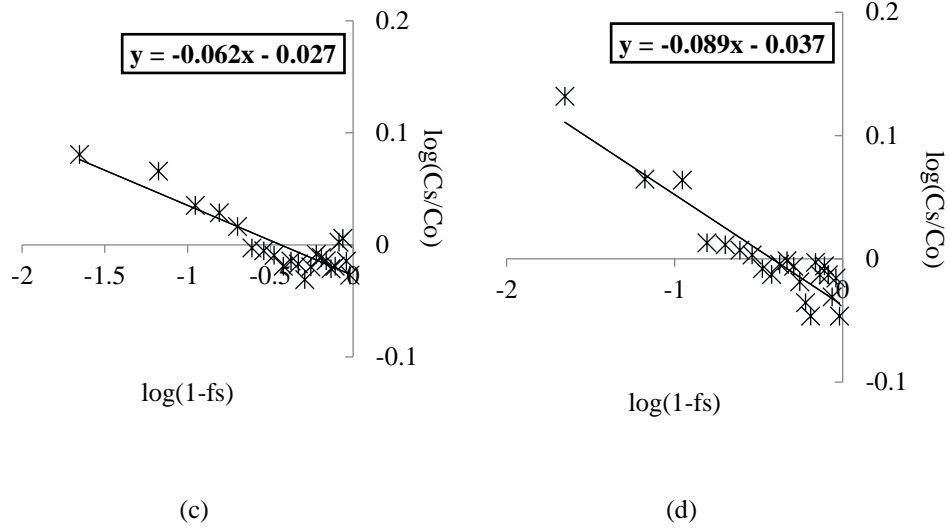


Figure 14 Longitudinal macrosegregation ( $C_s/C_o$ ) as a function of fraction solidified ( $f_s$ ) for Pb-6Sb grown at (a) 10.4  $\mu\text{m/s}$  (b) 63.1  $\mu\text{m/s}$  and corresponding  $\log(C_s/C_o)$  as a function of  $\log(1-f_s)$  for Pb-6Sb grown at (a) 10.4  $\mu\text{m/s}$  (b) 63.1  $\mu\text{m/s}$

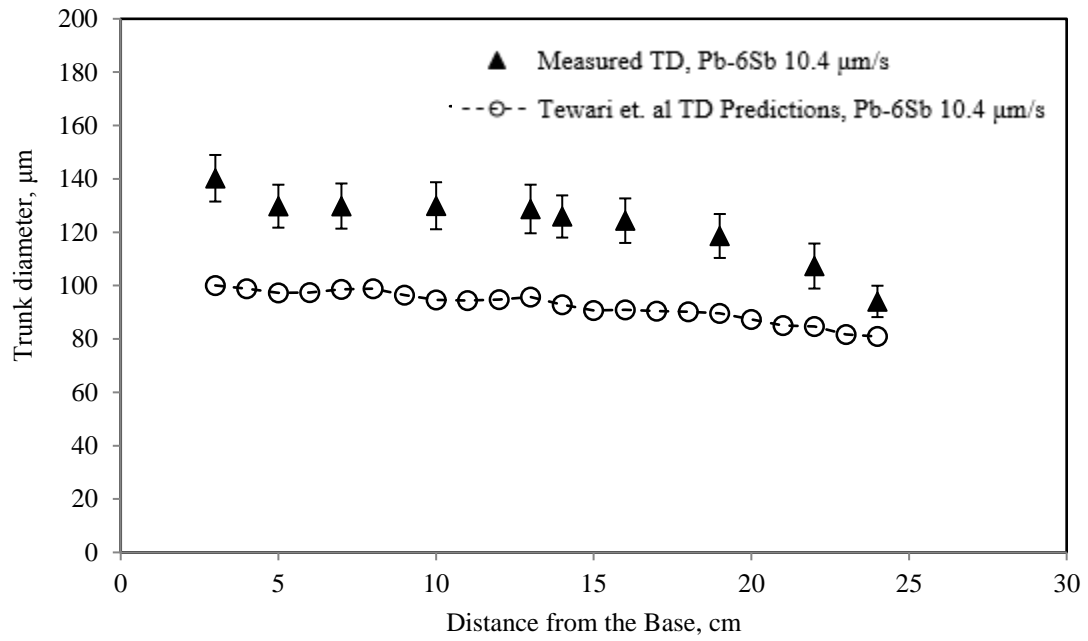
A  $C_s/C_o$  value of 1 suggests an absence of convection and therefore no macrosegregation. Figure - 14 (a) and (b) shows negative macrosegregation or  $C_s/C_o < 1$  initially until about 75% of the specimen grown at both 10.4 and 63.1  $\mu\text{m/s}$  were solidified. Positive macrosegregation or  $C_s/C_o > 1$  is observed as both specimen reach complete longitudinal solidification ( $f_s = 100\%$ ). The increasing trend for longitudinal macrosegregation was expected. As the liquid cools, the alpha phase dendrite of mostly Pb continuously rejects excess Sb and the remaining liquid becomes slightly richer in Sb as indicated by the liquidus line on the Pb-Sb phase diagram. The composition of the solid alpha phase also becomes slightly richer in Sb atoms as the solid solution line shows.

The effective partition coefficient,  $k_e$ , obtained by fitting experimentally observed macrosegregation to  $C_s/C_o = k_e (1-f_s)^{k_e-1}$  is a good indicator of the extent of convective mixing during directional solidification.<sup>19</sup> Figure - 14 (c) and (d) plots the  $\log(C_s/C_o)$  as a function of  $\log(1-f_s)$  for the data shown in Figure -14 (a) and (b), respectively. The observed macrosegregation data shows a good fit to the established relationship. Average

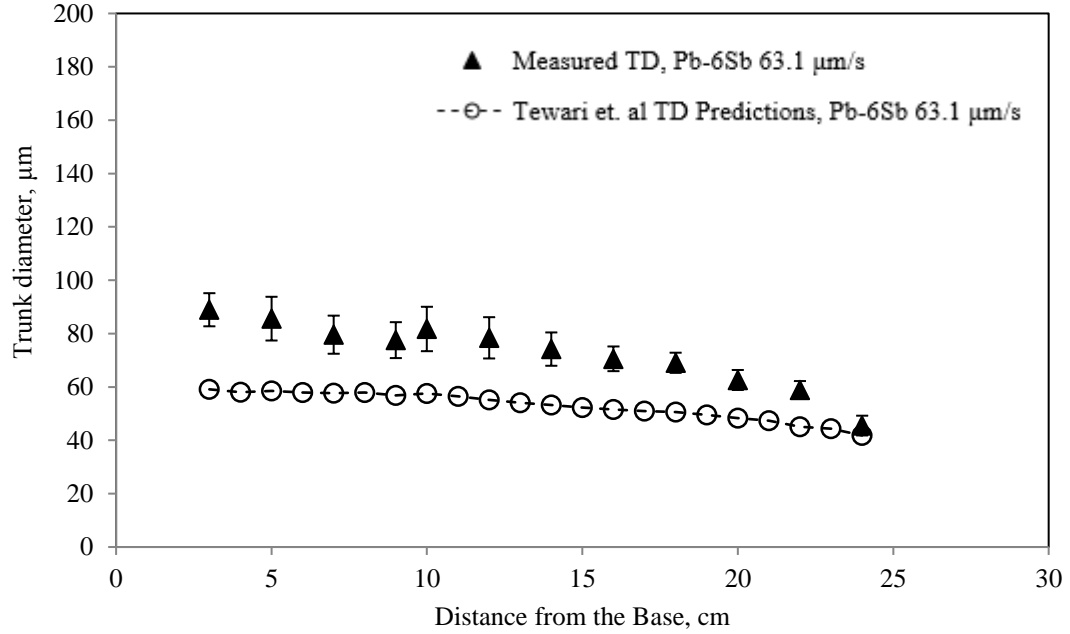
$k_e$  values obtained from the slope and that from the intercept for the specimen grown at 10.4 and 63.1  $\mu\text{m/s}$  are  $0.94 \pm 0.11$  and  $0.91 \pm 0.08$ , respectively. This suggests that a stronger convection may be present in the specimen grown at a lower growth speed.

### 3.1.3. Primary Dendrite Trunk Diameter Dependence on Growth Speed and Distance From the Base

The average trunk diameter values after solidification at several transverse locations were determined using the measured trunk diameter from transverse images at each corresponding locations. The dependence of average primary dendrite trunk diameter on distance from the base of the directionally solidified specimens with constant cross section grown at 10.4 and 63.1  $\mu\text{m/s}$  are plotted in Figures - 15 (a) and (b), respectively.



(a)



(b)

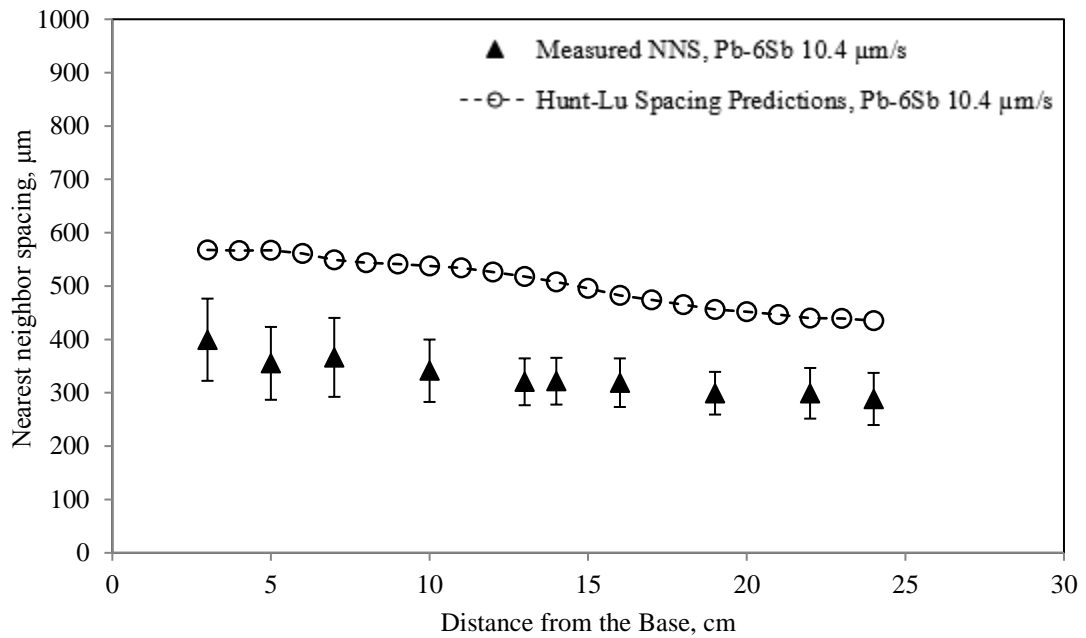
Figure 15 Average primary dendrite trunk diameter as a function of location for Pb-6Sb grown at (a) 10.4  $\mu\text{m/s}$  (b) 63.1  $\mu\text{m/s}$

The mean trunk diameter decreases as the distance from the base increase. This is indicative of the longitudinal macrosegregation due to thermo-solutal convection. The mean trunk diameter also decreases with increasing growth speeds. The results using the trunk diameter prediction model by Tewari et. al are also plotted in Figures - 15 (a) and (b).<sup>19</sup> The figures indicate that there is a good agreement between the model and experimental data even though the experimental data is consistently greater compared to the predicted values.

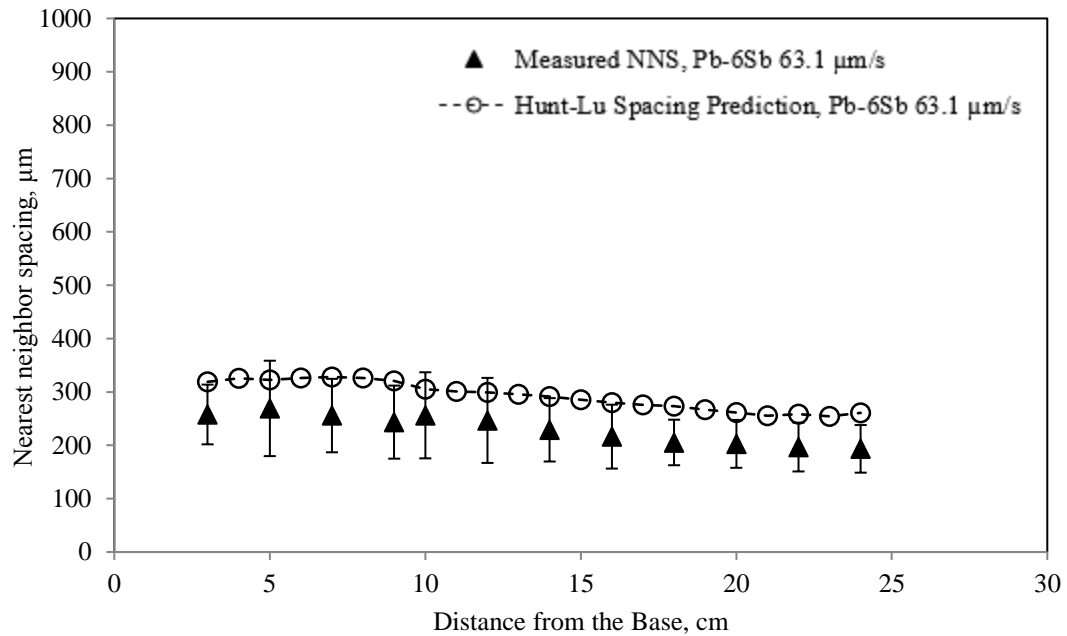
#### 3.1.4. Nearest Neighbor Spacing Dependence on Growth Speed and Distance From the Base

Nearest neighbor spacing (n.n. spacing) at various locations were calculated using the measured dendrite centers from transverse images at each corresponding locations. The n.n. spacing for specimens with constant cross section grown at 10.4 and 63.1  $\mu\text{m/s}$  are

plotted in Figures - 16 (a) and (b), respectively. The figures suggest increasing growth speed decreases n.n. spacing. The Hunt-Lu model allows for the calculation of primary spacing in a steady state growth system of dendrites in a moving linear temperature field as a function of distance.<sup>14,18</sup> The observed n. n. spacing in both specimens grown in 10.4 and 63.1  $\mu\text{m/s}$  growth speeds decrease as the distance from the base increases. The observed n. n. spacing values are also consistently lower than the predicted values for both specimens grown at 10.4 and 63.1  $\mu\text{m/s}$ .



(a)



(b)

Figure 16 Nearest neighbor spacing as a function of location for Pb-6Sb grown at (a) 10.4  $\mu\text{m/s}$  (b) 63.1  $\mu\text{m/s}$

### 3.2. Effects of Cross-section Contraction in Pb-6 % Sb (Solutally Unstable) vs.

#### Al-19 % Cu (Solutally Stable) Systems

##### 3.2.1. Longitudinal and Transverse Macrostructure Images

A longitudinal section through the Pb-6 % Sb specimen near the cross section contraction point (from 12.7 to 6.35 mm sample diameter) is shown in Figure - 17. This sample is solidified at a low growth speed of 11.5  $\mu\text{m/s}$ . The hot end of the sample is indicated by an arrow on the bottom left of the longitudinal section. A “eutectic” only region at the shelf-top immediately prior to the cross-section decrease can be observed. Some of the primary  $\alpha$  dendrites appear to continue on through the section decrease.

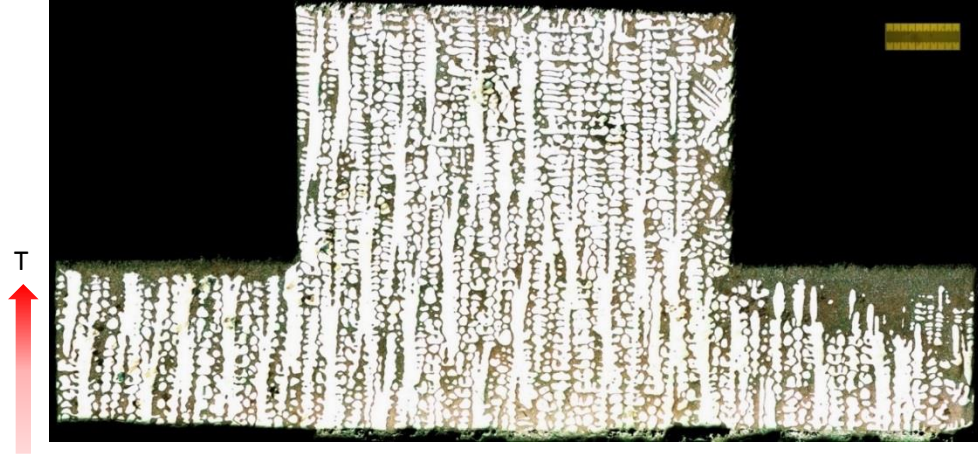


Figure 17 Longitudinal macrostructure of Pb-6Sb grown at 11.5  $\mu\text{m/s}$  with cross section contraction.  
(Diameter decrease from 12.7 mm to 6.35 mm)

Figure - 18 (a) shows the transverse images before and after contraction corresponding to the Pb-6 % Sb specimen seen in Figure - 17. Figure - 18 (b) shows the transverse images before and after contraction for Al-19% Cu grown at 11.5  $\mu\text{m/s}$  from a previous study conducted by Masoud et. al.<sup>11</sup> Negative distances represent transverse locations before the contraction and positive distances indicate transverse locations after contraction.



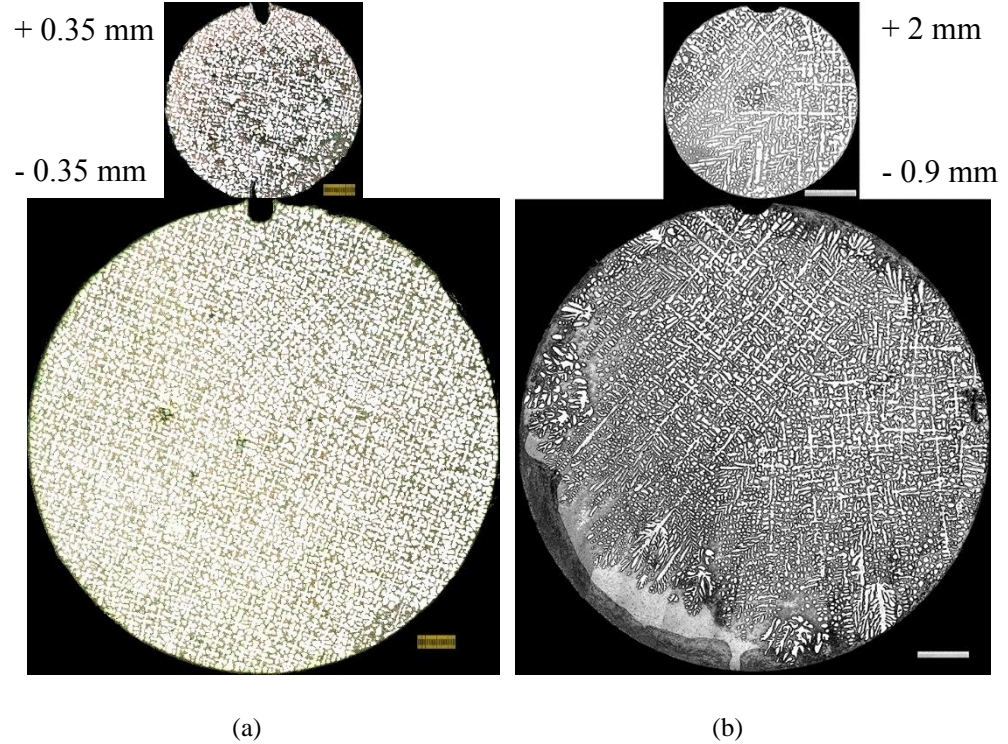


Figure 18 Transverse macrostructure of (a) Pb-6Sb grown and (b) Al-19Cu<sup>11</sup> at 11.5  $\mu\text{m/s}$  with cross section contraction.

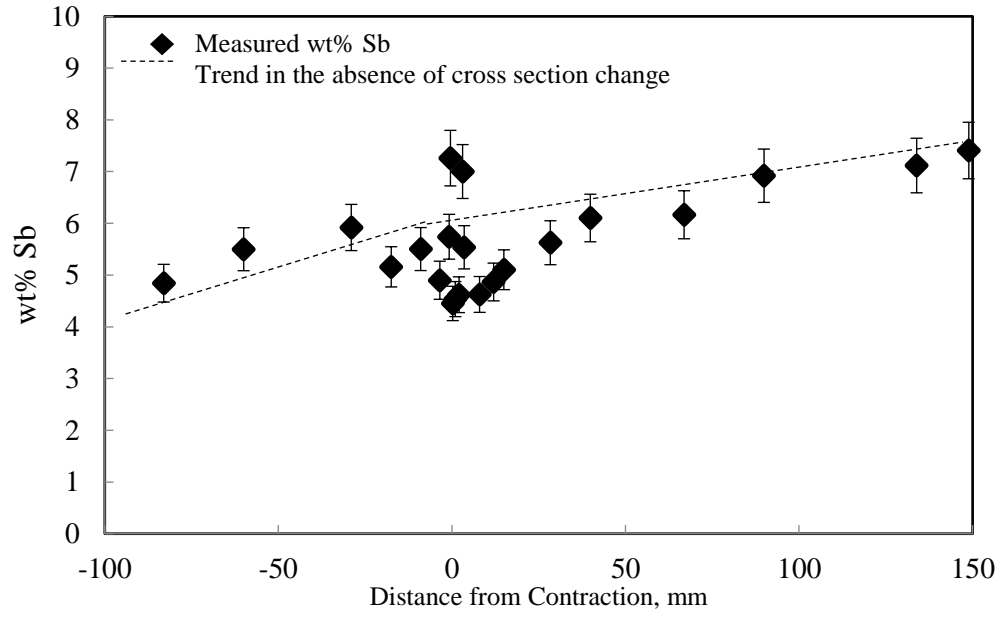
Radial macrosegregation is observed in Al-19 % Cu which is not present in the Pb-6 % Sb transverse macrostructure image. Some of the primary  $\alpha$  dendrites appear to continue on through the section decrease for both Pb-6 % Sb and Al-19 % Cu. Within the core, immediately after contraction, the transverse and longitudinal images for Pb-6% Sb show primarily dendrite  $\alpha$  phase and the channels which also appear to continue on through the section decrease. Channel flow in the liquid is likely to cause remelting and possible stray grain formation as observed in the misaligned dendrites immediately after contraction on the right side of the smaller diameter section as seen in Figure - 17. The presence of steeping convection in Al-19 % Cu is suggested from the eutectic-only region observed in the transverse image right before contraction. Steeping seems to disappear immediately

after contraction but should be noted that it re-establishes itself about +13 mm above the point of contraction.<sup>7,11</sup>

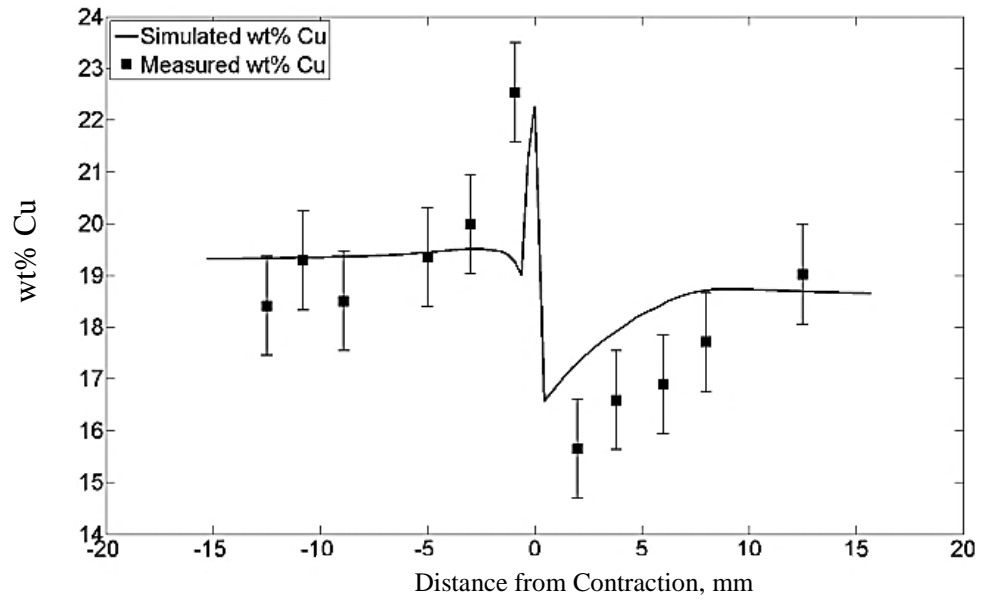
As the mushy-zone approaches contraction, the solute at the array tips gets accumulated on the top-shelf around the sample periphery causing solute accumulation before the cross-section change. Shrinkage flow from the smaller section is anti-parallel to the primary dendrite arms at the center of the section and may diverge towards the outer radius in the larger section. Radial macrosegregation can, therefore, be observed right before contraction for Pb-6% Sb due to solidification of entrapped solute-rich liquid as seen in Figure -17.

### **3.2.2. Comparison of Longitudinal Macrosegregation in Pb-6% Sb vs. Al-19% Cu Directionally Solidified with Cross-section Contraction**

Measurements of  $f_E$  in several transverse sections along the specimen length, before and after the contraction, were used to determine the solute concentration at each predetermined locations. The equations discussed in Sec. 3.13.2 were used to determine Sb concentration for Pb-6% Sb For Al-19% Cu,  $C_{0_{Cu}} = 4.408 + 28.86f_E$  was used<sup>8</sup> Figure-19 (a) illustrates the measured concentration of Sb and the general trend in the absence of a cross section contraction.



(a)



(b)

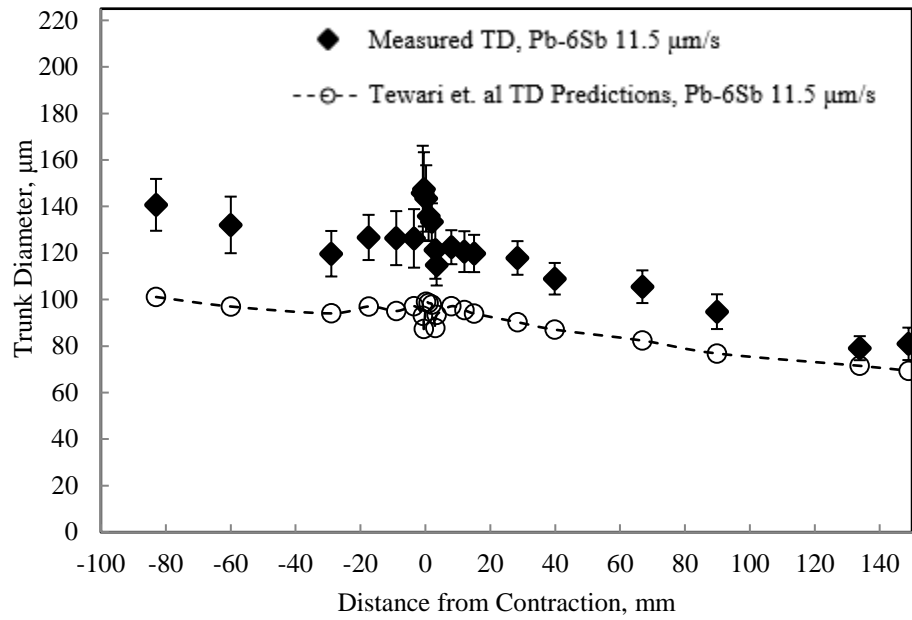
Figure 19 Longitudinal macrosegregation (%Solute) as a function of distance from contraction for (a) Pb-6 Sb and (b) Al-19Cu<sup>11</sup>

The gradual increase in concentration along the DS length suggests the presence of thermo-solutal convection allowing solute-rich interdendritic fluid to mix with the bulk

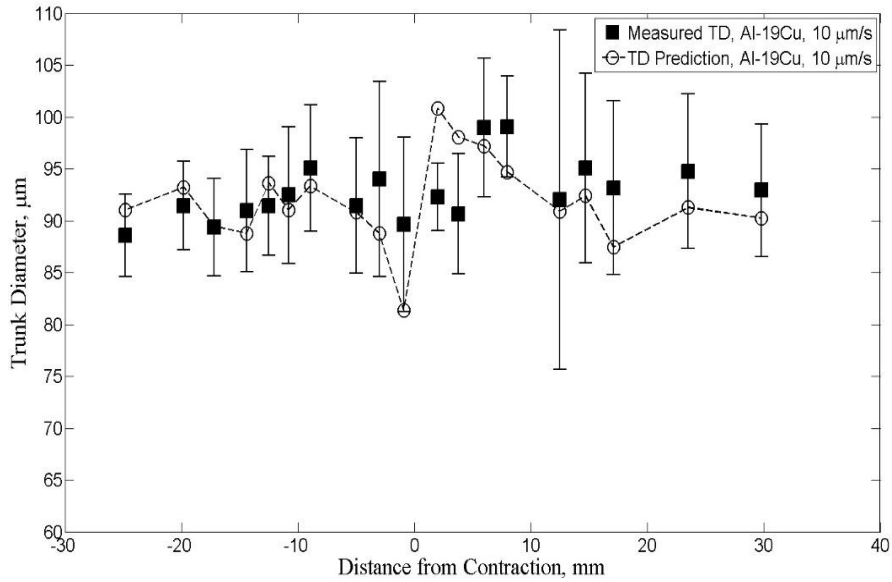
melt ahead of the mushy zone in Pb-6% Sb. This is seen in both the specimens where there is a presence of contraction and also where there is a uniform cross-section along the length. This is not seen in the experiments run by Masoud et. al for Al-19% Cu in the presence of contraction where there is minimal longitudinal macrosegregation as seen in Figure - 19 (b).<sup>11</sup> For both Pb-6% Sb and Al-19% Cu systems, a solute build-up is seen just before the contraction, which is followed by a sharp decrease just after the contraction. The solute content then slowly recovers after the contraction. This trend is supported by the longitudinal image shown in Figure - 17. This is because of the solute rich liquid ahead of the mushy-zone array getting trapped below the beginning of contraction on the ceilings in the mold below around the outer periphery.

### **3.2.3. Comparison of Primary Dendrite Trunk Diameter in Pb-6% Sb vs. Al-19% Cu Directionally Solidified with Cross-section Contraction**

Figure - 20 (a) shows the primary dendrite trunk diameter dependence on distance from the cross-section contraction for Pb-6% Sb. The plots also show the predicted trunk diameter using Tewari et al. model.<sup>19</sup> Experimental and predicted data for trunk diameter in Al-19 % Cu were obtained from Masoud et. al previous study and plotted in Figure - 20 (b) below.<sup>11</sup>



(a)



(b)

Figure 20 Average primary dendrite trunk diameter as a function of distance from contraction for (a) Pb-6Sb and (b) Al-19Cu<sup>11</sup>

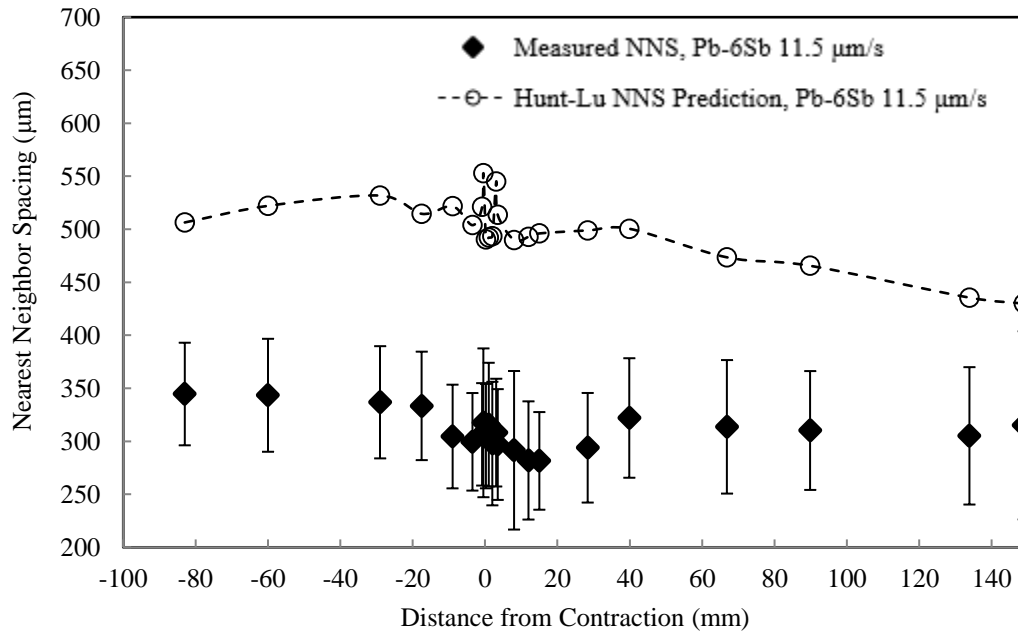
The average trunk diameter for Pb-6% Sb is observed to decrease over the entire length of the sample. This is indicative of the longitudinal macrosegregation caused by the presence of strong plume-type thermosolutal convection in the melt. This trend is not seen

in the Al-19% Cu, where the trunk diameter remains relatively constant over the length of the specimen through a contraction. Right at the contraction, the area-change-driven shrinkage flow slightly decreases the trunk diameter for Pb-6% Sb. The measured trunk diameter is consistently larger than the predicted values for Pb-6% Sb but fits the model very well in the Al-19% Cu.

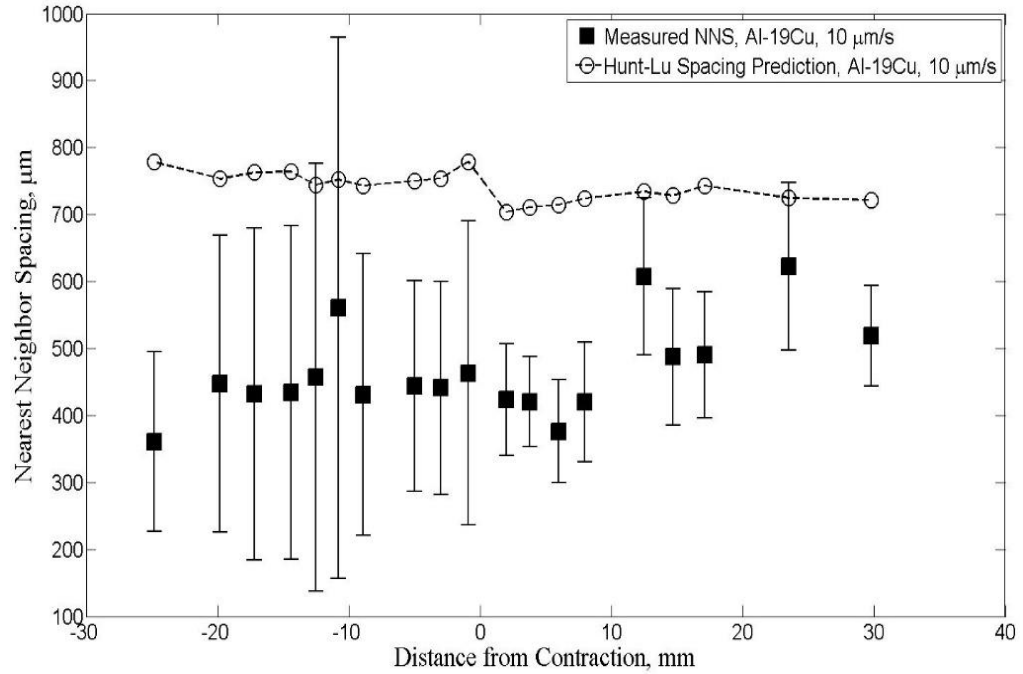
### 3.2.4. Comparison of Nearest Neighbor Spacing in Pb-6% Sb vs. Al-19%

#### Cu Directionally Solidified with Cross-section Contraction

The dependence of nearest neighbor spacing (n.n. spacing) on distance from the contraction was plotted for Pb-6% Sb in Figure-21 (a). Predicted n.n. spacing values were calculated using Hunt-Lu model also shown in the plots below.<sup>14,18</sup> Experimental and predicted data for n. n. spacing values for Al-19 % Cu were obtained from Masoud et. al previous study and plotted in Figure - 21 (b) below.<sup>11</sup>



(a)



(b)

Figure 21 Nearest neighbor spacing as a function of distance from contraction for (a) Pb-6Sb and (b) Al-19Cu<sup>11</sup>

The experimental n. n. spacing values for both Pb-6% Sb and Al-19% Cu are consistently lower than the model calculations. At the contraction, the predicted n.n. spacing in the Pb-6% Sb shows an increase that is not seen in the experimental data. There is a slight decrease in the measured n. n. spacing starting from about -20 mm before the contraction which quickly increases back at about 10 mm after contraction. Area-change-driven shrinkage flow has a more observable effect on the n.n. spacing close to the contraction point for Pb-6% Sb than Al-19% Cu.

### 3.3. Effects of Cross-Section Expansion in Pb-6% Sb (Solutally Unstable) vs. Al-19% Cu (Solutally Stable) Systems

#### 3.3.1. Longitudinal and Transverse Macrostructure Images

A longitudinal section through the Pb-6% Sb specimen near the cross section expansion point (from 6.35 mm to 12.7 sample diameter) is shown in Figure - 22. Primary  $\alpha$  phase fills the diameter immediately following the expansion. Some of the primary  $\alpha$  dendrites from the smaller cross section region appear to continue on through the section increase. New dendrites formed in the expanded region also grew in alignment with the existing core dendrites. There are no misaligned dendrites observed in the reentrant of the cross-section expansion. This is very different than Masoud et. al.<sup>11</sup> observation in Al-19%Cu alloy where extensive new grain formation was observed on the expansion platform above.



Figure 22 Longitudinal macrostructure of Pb-6Sb grown at 8.7  $\mu\text{m/s}$  with cross section expansion. (Diameter increase from 6.35 mm to 12.7 mm)

Figure 23 (a) shows the transverse images before and after expansion corresponding to the Pb-6 % Sb specimen seen in Figure - 22. Figure - 22 (b) shows the transverse images before and after contraction for Al-19% Cu grown at 10  $\mu\text{m/s}$  from a previous study conducted by Masoud et. al.<sup>11</sup> It is evident that in Pb-6% Sb alloy no new grains were formed whereas extensive “spurious grains” were observed to form in Al-19% Cu alloy samples. It may be because the dendrite fragments resulting from the localized convection induced solutal-remelting of slender side-branches which act as nuclei for the formation of potential spurious grains are denser than the surrounding liquid melt in the case of Pb-6% Sb alloy and therefore sink and get entrapped in the growing dendrite network. This may not be the case with the Al-19% Cu alloy, where the broken primary  $\alpha$ -phase dendrite



fragments have a lower density than the surrounding melt. Hence, they float and depending upon the local thermal conditions some of them may grow into new misoriented grains.

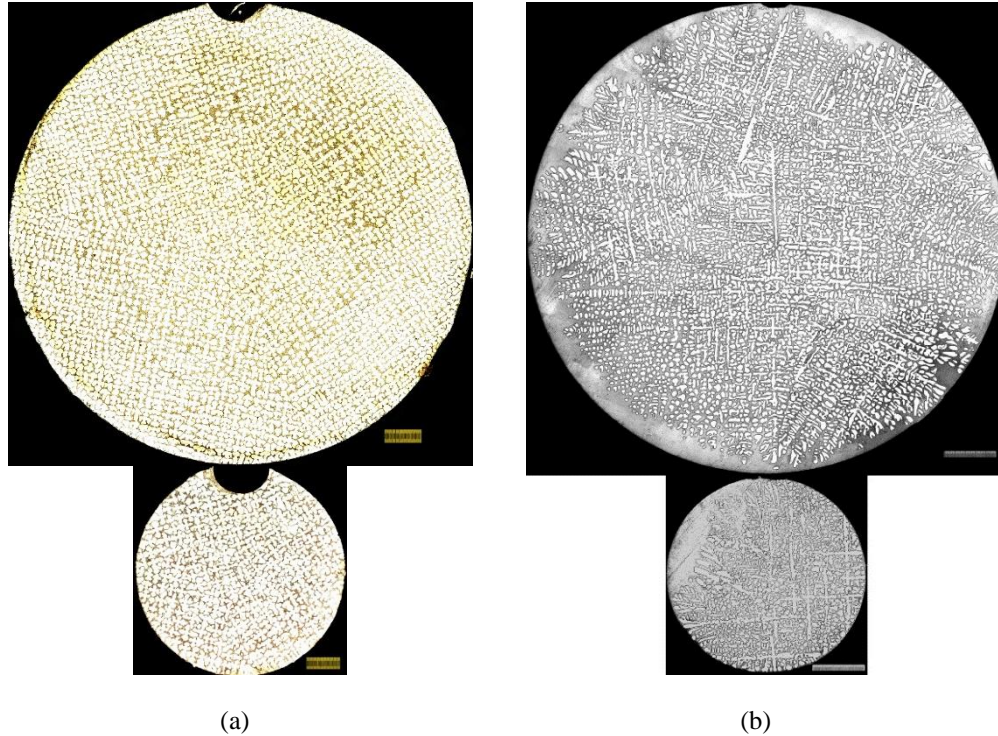
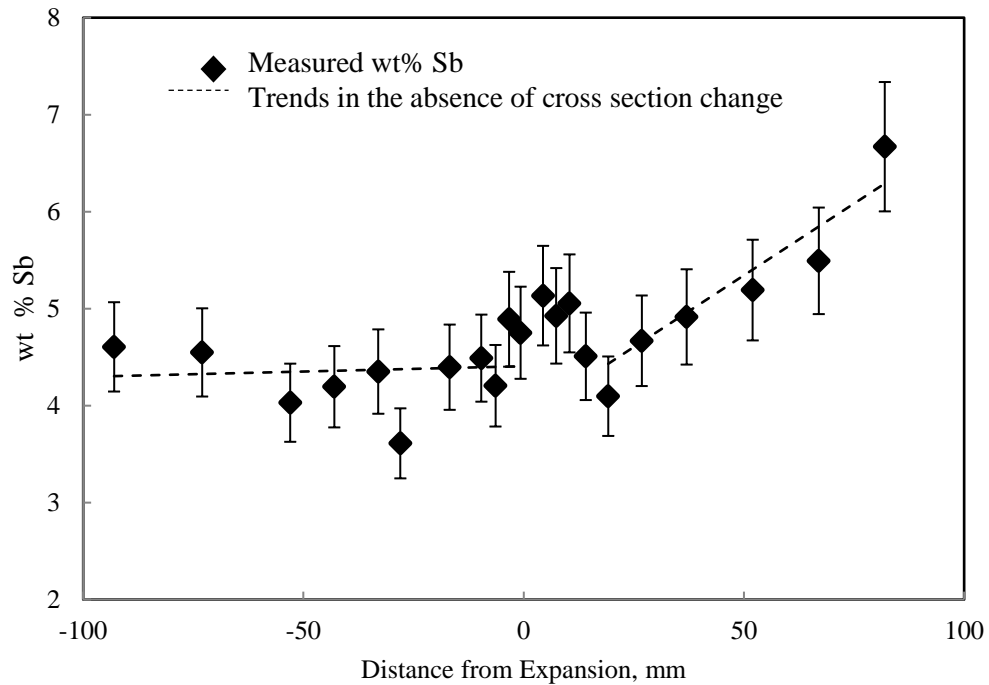


Figure 23 Transverse macrostructure of (a) Pb-6Sb grown at  $8.7 \mu\text{m/s}$  and (b) Al-19Cu<sup>11</sup> at  $10 \mu\text{m/s}$  with cross section expansion.

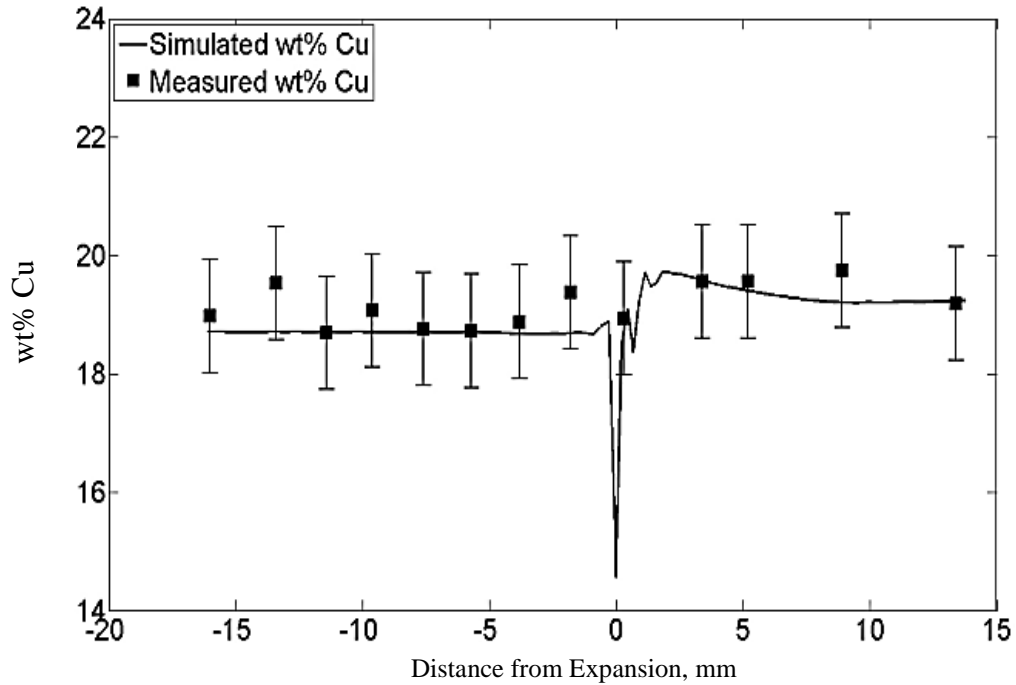
### 3.3.2. Longitudinal Chemical Inhomogeneity

Longitudinal macrosegregation in Pb-6% Sb grown at  $8.7 \mu\text{m/s}$  as a function of distance from the cross section expansion is plotted in Figure - 24 (a). The gradual increase in Sb concentration is indicative of the presence of convection. The expected trend in the absence of an expansion is also plotted in Figure - 24 (a) with a dashed line. The slope of the expected trend in the larger cross section area is steeper than that in the smaller cross section area prior to expansion. This suggests that there is more macrosegregation in the larger cross section area after expansion than in the smaller cross section before. There is slight positive macrosegregation just before the cross section expansion as seen from the

experimental data. The reason for this behavior is not clear at this stage. It may have something to do with the weakening of the down-wards “solidification shrinkage” flow in this region. There is a negative macrosegregation immediately after the expansion because the side-branches of primary dendrites growing sideways and filling the platform above do not allow solute accumulation on the platform, the solute rejected by solidification is instead transported and mixed in the liquid column above. This spread of solute poor primary  $\alpha$  phase which solidified on the re-entrant shelf in the larger cross section region above is evident in the longitudinal microstructure image shown in Figure - 22.



(a)



(b)

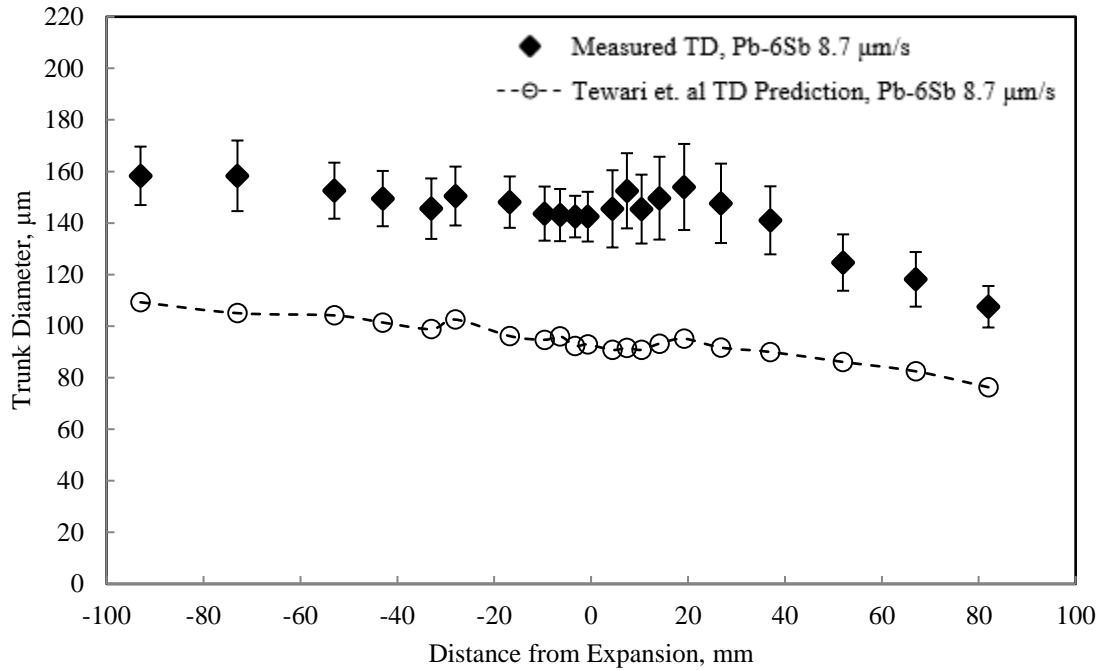
Figure 24 Longitudinal macrosegregation (%Solute) as a function of distance from expansion for (a) Pb-6 Sb and (b) Al-19Cu<sup>11</sup>

Figure - 24(b) shows the plot for longitudinal macrosegregation for Al-19 % Cu grown at  $8.7 \mu\text{m/s}$  as a function of distance from the cross section expansion as obtained results from a previous study.<sup>11</sup> Because in Al-19%Cu alloy the solute in the mushy-zone does not mix with the melt column above there is no longitudinal macrosegregation along the sample length. Average solute content along the sample length remains relatively unaffected by the section-change, except for the negative macrosegregation seen at the expansion platform above for the same reason as in the Pb-6%Sb alloy, the sideways spread of side-branches of primary dendrites.

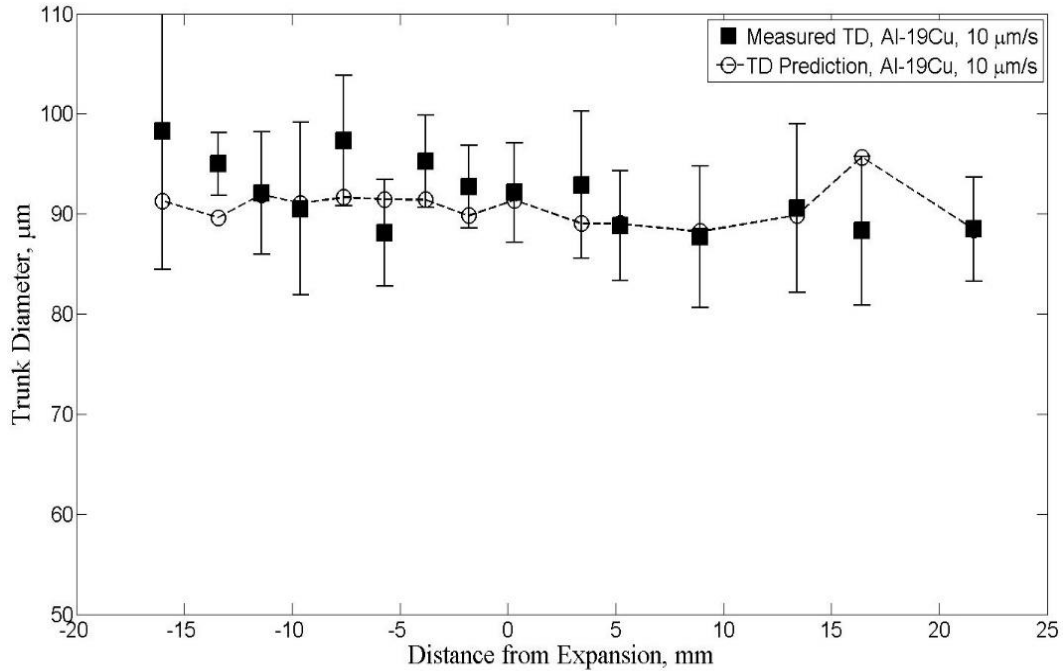
### 3.3.3. Primary Dendrite Trunk Diameter

Experimental and predicted primary dendrite trunk diameter results are plotted below for Pb-6% Sb (Figure - 25 (a)) and Al-19% Cu (Figure - 25 (b)) was obtained from

Masoud et al results) grown at  $8.7 \mu\text{m/s}$  as a function of distance from cross-section expansion.<sup>11</sup> The measured data for Pb-6% Sb are consistently larger than the predicted values. Since some of the primary  $\alpha$  dendrites from the smaller cross section region appear to continue on through the section increase (Figure - 22), cross-section expansion had little effect on trunk diameter measurements unlike in contraction. The resulting experimental trunk diameter for Al- 19% Cu seem to fit the predicted model well. This maybe in part due to the fact that convection in Al-19% Cu occurs radially and therefore might be minimized longitudinally.



(a)

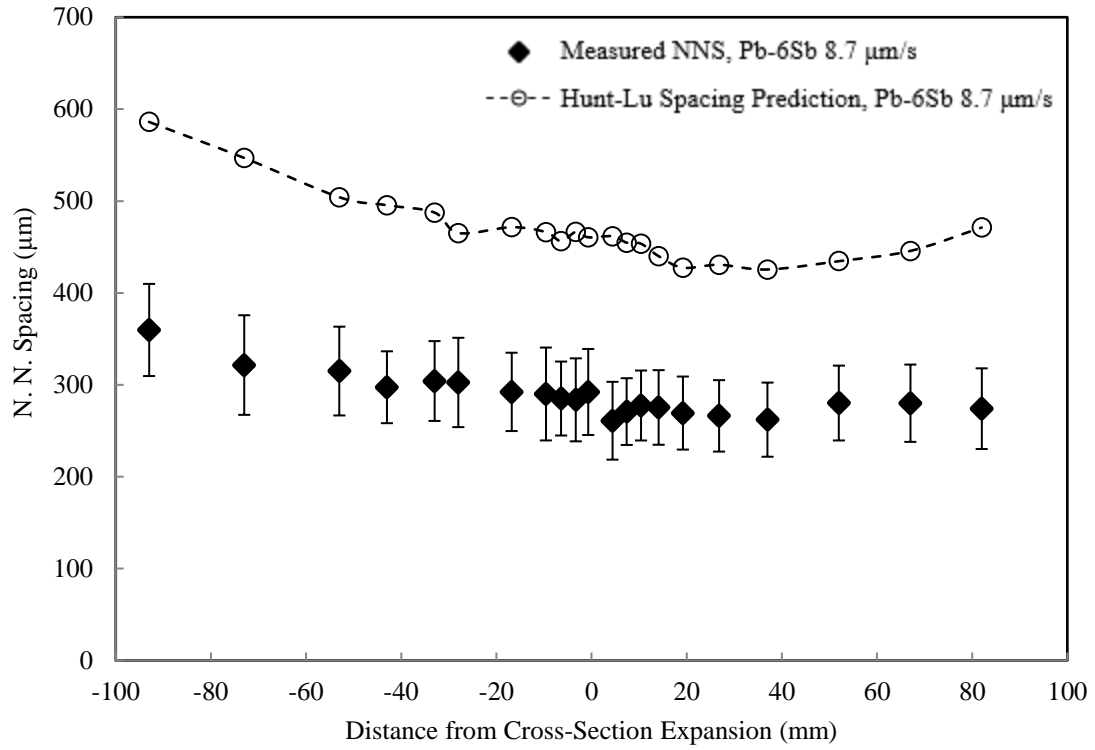


(b)

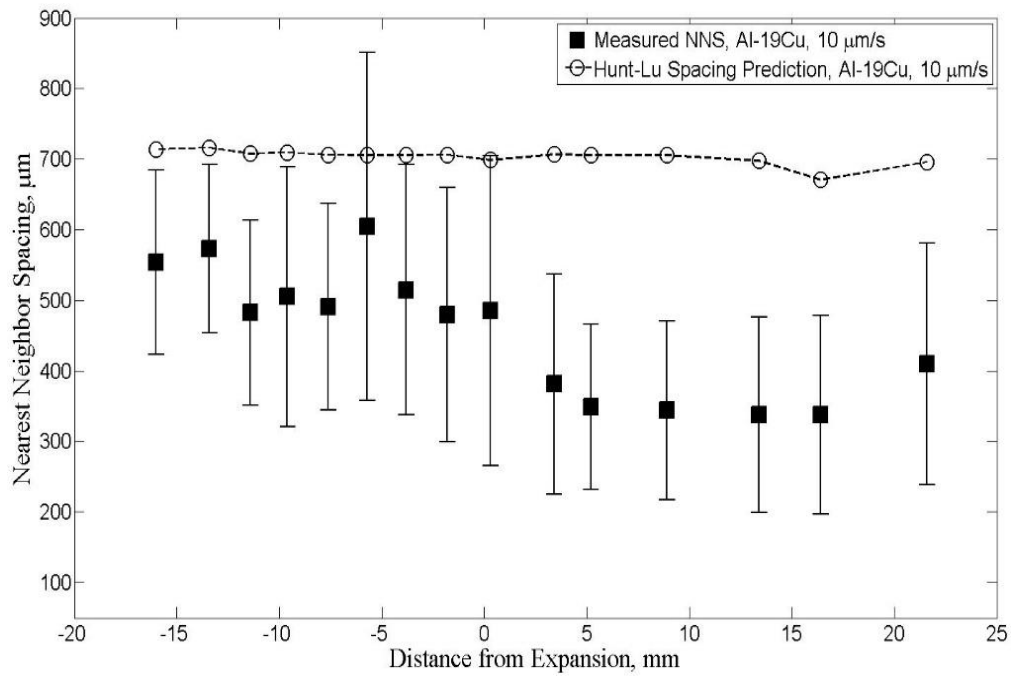
Figure 25 Primary dendrite trunk diameter as a function of distance from expansion for (a) Pb-6 Sb and (b) Al-19Cu<sup>11</sup>

### 3.3.4. Nearest Neighbor Spacing

The experimental and predicted primary dendrites nearest neighbor spacing for Pb-6% Sb and Al-19% Cu results from the previous experiment are plotted in Figure - 26 (a) and (b), respectively as a function of distance from expansion.<sup>11</sup> In both systems, the measured nearest neighbor spacing is lower than the predicted values from the Hunt-Lu equation. A slight decrease in spacing can also be noted after expansion for both Pb-6% Sb and Al-19% Cu. This may have been caused by area-change-driven shrinkage flow that is not as intensified in expansion as it is in a contraction abrupt change.



(a)



(b)

Figure 26 Nearest neighbor spacing as a function of distance from expansion for (a) Pb-6 Sb and (b) Al-19Cu<sup>11</sup>

## **CHAPTER IV**

### **CONCLUDING REMARKS**

In summary, Pb-6% Sb alloy cylindrical samples were directionally solidified in 9 mm diameter constant cross-section mold and also in molds having an abrupt cross-section decrease (from 9-mm to 3.2 mm) and also an abrupt cross-section increase (from 3.2 mm to 9-mm) for growth 10.4, 63.1., 11.5 and 8.7  $\mu\text{m/s}$  growth speeds, respectively. This alloy system is susceptible to “plume type” of thermosolutal convection because of the solute-concentration induced melt density inversion in the interdendritic melt in the mushy zone. Mushy zone morphology along the length of the samples was metallographically examined and analyzed using quantitative image-analysis techniques. The longitudinal and radial chemical inhomogeneities (macrosegregation) were measured on several transverse sections along the sample length. Primary dendrite nearest neighbor spacing and primary dendrite trunk diameters were also measured on these transverse sections. The experimental observations were compared with those made by Masoud et. al<sup>11</sup> in Al-19%Cu alloy which is not susceptible to “plume type” of thermosolutal convection. Instead, it is susceptible to “Steepling type” of thermosolutal convection. Following conclusions can be made from this study.

In the constant cross-section samples,

1. In the directionally solidified Pb-6% Sb alloy, the experimentally measured primary dendrite trunk diameter values are higher than those predicted from theoretical models which do not take convection into account. This is not the case with Al-19% Cu alloy.
2. In the directionally solidified Pb-6% Sb alloy, the experimentally measured primary dendrite nearest neighbor spacings are lower than those predicted from theoretical models which take only diffusive transports into consideration. This is also the case with the Al-19% Cu alloy.
3. Longitudinal macrosegregation caused by convective mixing of the interdendritic mushy zone melt with the bulk melt above is observed in the Pb-6% Sb alloy samples. The Al-19% Cu alloy samples did not show any longitudinal macrosegregation.
4. It appears that the slower growth speed results in more convective mixing and thus a slightly larger extent of longitudinal macrosegregation (slope of  $\log(C_s/C_o)$  vs.  $\log(1-f_s)$ ) in Pb-6%Sb alloy.

In the Cross-section change samples,

1. For the abrupt cross section area decrease, both solutally stable (Al-19% Cu) and unstable (Pb-6% Sb) alloy samples showed an increase in macrosegregation due to the solute rich liquid ahead of the solidifying mushy zone below getting entrapped at the bottom of the expansion shelf just before the cross section change. This is followed by a solute concentration decrease after the section change, possibly because of the solidifying shrinkage fluid flow intensifying as the liquid-solid



interface approaches the section decrease.

2. For the abrupt cross-section area increase, there is a solute depletion just ahead of the section change because in this region the primary dendrite arrays emerging from below shoot-off side-branches which grow side-ways and fill the larger cross-section platform above. This spreading primary  $\alpha$ -phase spreading on the platform above is solute poor. This is observed in both Pb-6% Sb and in Al-19% Cu alloy.
3. Al-19% Cu alloy sample showed extensive spurious grain formation on the platform above in the samples solidifying through an abrupt area increase. This is not the case with Pb-6% Sb alloy samples. It may be because the dendrite fragments resulting from the localized convection induced solutal-remelting of slender side-branches which act as nuclei for the formation of spurious grains are denser than the surrounding liquid in the case of Pb-6% Sb alloy; which is not the case with the Al-19% Cu alloy.

## **CHAPTER V**

### **RECOMMENDATIONS FOR FUTURE RESEARCH**

1. Samples with a varying cross-section ratios should be examined to examine the role of section-change induced solidification shrinkage flow on the macrosegregation and dendritic array microstructure. Also samples with gentler cross-section change should be grown and studied.
2. A range of different alloy compositions and alloy systems need to be examined in order to better understand the role of alloy thermophysical properties.
3. Low-g experiments are required to isolate the “area-change induced” shrinkage flow and gravity driven thermosolutal convection flows on the dendritic array morphology and macrosegregation.

## REFERENCES

1. Al-Rawahi N, Tryggvason G. Numerical simulation of dendritic solidification with convection: Three-dimensional flow. *Journal of Computational Physics*. 2004;194(2):677-696. doi: <http://dx.doi.org/10.1016/j.jcp.2003.09.020>.
2. Dong H. Analysis of grain selection during directional solidification of gas turbine blades. *Proceedings of the World Congress on Engineering*. 2007.
3. Gell M, Duhl DN, Giamei A. The development of single crystal superalloy turbine blades. *Superalloys 1980*. 1980.
4. Dong H, Dai H, Geblin J, et al. Grain selection during solidification in spiral grain selector. *Journal of the Minerals, Metals and Materials Society*. 2008:367-374.
5. Pollock TM, Murphy WH, Goldman EH, Uram DL, Tu JS. Grain defect formation during directional solidification of nickel base single crystals. *Superalloys 1992*. 1992.
6. Flemings M. *Solidification processing*. ; 1974.
7. Ghods M, Johnson L, Lauer M, Grugel RN, Tewari SN, Poirier DR. Radial macrosegregation and dendrite clustering in directionally solidified Al–7Si and Al–19Cu alloys. *Journal of Crystal Growth*. 2016;441:107-116. doi: <http://dx.doi.org/10.1016/j.jcrysgro.2016.02.014>.

8. Johnson L. *Analysis of microstructure and macrosegregation for directional solidification of al-7 wt% si alloy with A cross-section change at growth speeds of 10 and 29.1  $\mu\text{m}/\text{S}$* . Cleveland State University; 2012.
9. Flemings M, Nereo G, Mehrabian R. Macrosegregation: Part II. *Trans. TMS-AIME*. 1968;242:41-49.
10. Flemings M, Nereo G. Macrosegregation: Part III. *Trans. TMS-AIME*. 1968;242:50-55.
11. Ghods M, Lauer M, Grugel RN, Tewari SN, Poirier DR. Convection and macrosegregation in al-19Cu alloy directionally solidified through an abrupt contraction in cross-section: A comparison with al-7Si. *Journal of Crystal Growth*. 2017;459:135-145. doi: <http://dx.doi.org/10.1016/j.jcrysgro.2016.11.111>.
12. Ma D, Ziehm J, Wang W, Bührig-Polaczek A. Freckle formation in directionally solidified superalloy components with expanding cross-section. . 2012.
13. Kurz W, Fisher DJ. Dendrite growth at the limit of stability: Tip radius and spacing. *Acta Metallurgica*. 1981;29(1):11-20. doi: [http://dx.doi.org/10.1016/0001-6160\(81\)90082-1](http://dx.doi.org/10.1016/0001-6160(81)90082-1).
14. Lu S, Hunt JD. A numerical analysis of dendritic and cellular array growth: The spacing adjustment mechanisms. *Journal of Crystal Growth*. 1992;123(1):17-34. doi: [http://dx.doi.org/10.1016/0022-0248\(92\)90006-5](http://dx.doi.org/10.1016/0022-0248(92)90006-5).

15. Zhao P, Heinrich J,C., Poirier D,R. *Dendritic solidification of binary alloys with free and forced convection*. Vol 49. ; 2005:233-266. 10.1002/fld.988.
16. Katz RF, Worster MG. Simulation of directional solidification, thermochemical convection, and chimney formation in a hele-shaw cell. *Journal of Computational Physics*. 2008;227(23):9823-9840. doi: <http://dx.doi.org/10.1016/j.jcp.2008.06.039>.
17. Trivedi R, Mason JT, Verhoeven JD, Kurz W. Eutectic spacing selection in lead-based alloy systems. *Metallurgical Transactions A*. 1991;22(10):2523-2533.
18. Hunt JD, Lu S. Numerical modelling of cellular and dendritic array growth: Spacing and structure predictions. *Materials Science and Engineering: A*. 1993;173(1):79-83. doi: [http://dx.doi.org/10.1016/0921-5093\(93\)90191-G](http://dx.doi.org/10.1016/0921-5093(93)90191-G).
19. Tewari SN, Grugel RN, Poirier DR. An evaluation of primary dendrite trunk diameters in directionally solidified al-si alloys. *Journal of Light Metals*. 2014;45(11):4758-4761.
20. Osório WR, Rosa DM, Garcia A. The roles of cellular and dendritic microstructural morphologies on the corrosion resistance of Pb–Sb alloys for lead acid battery grids. *Journal of Power Sources*. 2008;175(1):595-603. doi: <http://dx.doi.org/10.1016/j.jpowsour.2007.08.091>.
21. Flemings M, Nereo G. Macrosegregation: Part I. *Trans. TMS-AIME*. 1967;239:1449.

22. Tewari S, Shah R. Macroseggregation during dendritic array arrayed growth of hypoeutectic pb-sn alloys: Influence of primary arm spacing and mushy zone length. *Metall. Mater. Trans.A*. 1996;27A(5).
23. Kaya H, Cadirli E, Gunduz M. Dendritic growth in an aluminum-silicon alloy. *Journal of Materials Engineering and Performance*. 2007;16(1):12-21.
24. Tewari SN, Shah R, Chopra MA. Thermosolutal convection and macroseggregation. *Metallurgical Transactions A*. 1993;24(7):1661-1669.
25. Trivedi R, Miyahara H, Mazumder P, Simsek E, Tewari SN. Directional solidification microstructures in diffusive and convective regimes. *Journal of Crystal Growth*. 2001;222(1):365-379. doi: [http://dx.doi.org/10.1016/S0022-0248\(00\)00761-2](http://dx.doi.org/10.1016/S0022-0248(00)00761-2).
26. Pakiru S. *Effect of step change in growth speed during directional solidification on array morphology of al-7 wt% si alloy*. Cleveland State University; 2011.
27. Chen J, Tewari S, Magadi G, De Groh H. *Effect of crucible diameter reduction on the convection, macroseggregation, and dendritic morphology during directional solidification of pb-2.2 wt pct sb alloy*. Vol 34. ; 2003:2985-2990. 10.1007/s11661-003-0197-7.
28. Trivedi R, Liu S, Mazumder P, Simsek E. Microstructure development in the directionally solidified Al-4.0wt% cu alloy system. *Science and Technology of Advanced Materials*. 2001;2(1):309-320. doi: [http://dx.doi.org/10.1016/S1468-6996\(01\)00062-6](http://dx.doi.org/10.1016/S1468-6996(01)00062-6).

29. Sarazin J, Hellawell A. Channel formation in pb-sn, pb-sb, and pb-sn-sb alloy ingots and comparison with the system  $\text{NH}_4\text{Cl-H}_2\text{O}$ . *Trans. TMS-AIME*. 1988;19A.

## APPENDIX A

### TRUNK DIAMETER AND NEAREST NEIGHBOR SPACING MATLAB CODE

#### CALCULATIONS USING EXPERIMENTAL DATA

```
clc; clear all
ExcelFile= uigetfile;
raw=xlsread(ExcelFile); %% the numerical values in a matrix called raw
[r c]=size(raw); % r is number of rows and c is number of columns in
data excel file
scale=2420; % number of pixels per mm in original image

%% the for loop scans pairs of line in "raw" matrix
for n=1:r/2

    % this if takes care of the regular drawn lines. The sixth element
    of
    % each row is the angle and decision about the use of BX and BY as
    a known point
    % on the drawn line is based on this angle value

    if ((raw(2*n-1,6)<0) && (raw(2*n-1,6)> -90)) || ((raw(2*n-1,6)> 90)
    && (raw(2*n-1,6)< 180))
        X1=raw(2*n-1,2);
        Y1=raw(2*n-1,3);
        X2=raw(2*n,2);
        Y2=raw(2*n,3)+raw(2*n,5);
        m1=-tand(raw(2*n-1,6));
        m2=-tand(raw(2*n,6));
        X=(m1*X1-Y1+Y2-m2*X2)/(m1-m2);
        Y=m1*(X-X1)+Y1;
        TD=(raw(2*n-1,7)+raw(2*n,7))/2/(scale/1000);

    else if ((raw(2*n-1,6)<90) && (raw(2*n-1,6)> 0)) || ((raw(2*n-1,6)>
    -180) && (raw(2*n-1,6)< -90))
        X1=raw(2*n-1,2);
        Y1=raw(2*n-1,3)+raw(2*n-1,5);
        X2=raw(2*n,2);
        Y2=raw(2*n,3);
        m1=-tand(raw(2*n-1,6));
        m2=-tand(raw(2*n,6));
        X=(m1*X1-Y1+Y2-m2*X2)/(m1-m2);
        Y=m1*(X-X1)+Y1;
        TD=(raw(2*n-1,7)+raw(2*n,7))/2/(scale/1000);
    end
end

%%%%%% special cases start here %%%%%%%%%

% this if makes decision about the use of BX and BY in case the
first line in a pair is vertical
% and the second one is either in first or in third quadrant
```



```

        if ((row(2*n-1,6)== 90) || (row(2*n-1,6)== -90)) &&
        (((row(2*n,6)<90) && (row(2*n,6)> 0)) || ((row(2*n,6)> -180) &&
        (row(2*n,6)< -90)))
            X2=row(2*n,2);
            Y2=row(2*n,3)+row(2*n,5);
            m2=-tand(row(2*n,6));
            X=row(2*n-1,2);
            Y=m2*(X-X2)+Y2;
            TD=(row(2*n-1,7)+row(2*n,7))/2/(scale/1000);
        end

        % this if makes decision about the use of BX and BY in case the
        first line in a pair is vertical
        % and the second one is either in forth or in second quadrant
        if ((row(2*n-1,6)== 90) || (row(2*n-1,6)== -90)) &&
        (((row(2*n,6)<0) && (row(2*n,6)> -90)) || ((row(2*n,6)> 90) &&
        (row(2*n,6)< 180)))
            X2=row(2*n,2);
            Y2=row(2*n,3);
            m2=-tand(row(2*n,6));
            X=row(2*n-1,2);
            Y=m2*(X-X2)+Y2;
            TD=(row(2*n-1,7)+row(2*n,7))/2/(scale/1000);
        end

        % this if makes decision about the use of BX and BY in case the
        first
        % line in a pair is horizontal
        % and the second one is either in first or in third quadrant
        if ((row(2*n-1,6)== 0) || (row(2*n-1,6)== 180)) &&
        (((row(2*n,6)<90) && (row(2*n,6)> 0)) || ((row(2*n,6)> -180) &&
        (row(2*n,6)< -90)))
            X2=row(2*n,2);
            Y2=row(2*n,3)+row(2*n,5);
            m2=-tand(row(2*n,6));
            Y=row(2*n-1,3);
            X=(Y-Y2)/m2+X2;
            TD=(row(2*n-1,7)+row(2*n,7))/2/(scale/1000);
        end

        % this if makes decision about the use of BX and BY in case the
        first
        % line in a pair is horizontal
        % and the second one is either in forth or in second quadrant
        if ((row(2*n-1,6)== 0) || (row(2*n-1,6)== 180)) && (((row(2*n,6)<0)
        && (row(2*n,6)> -90)) || ((row(2*n,6)> 90) && (row(2*n,6)< 180)))
            X2=row(2*n,2);
            Y2=row(2*n,3);
            m2=-tand(row(2*n,6));
            Y=row(2*n-1,3);
            X=(Y-Y2)/m2+X2;
            TD=(row(2*n-1,7)+row(2*n,7))/2/(scale/1000);
        end

        % this if makes decision about the use of BX and BY in case the
        first

```

```

    % line in a pair is horizontal
    % and the second one is vertical
    if ((row(2*n-1,6)== 0) || (row(2*n-1,6)== 180)) && ((row(2*n,6)==
90) || (row(2*n,6)== -90))
        X=row(2*n,2);
        Y=row(2*n-1,3);
        TD=(row(2*n-1,7)+row(2*n,7))/2/(scale/1000);
    end

    % this if makes decision about the use of BX and BY in case the
first
    % line in a pair is vertical
    % and the second one is horizontal
    if ((row(2*n-1,6)== 90) || (row(2*n-1,6)== -90)) && ((row(2*n,6)==
0) || (row(2*n,6)== 180))
        X=row(2*n-1,2);
        Y=row(2*n,3);
        TD=(row(2*n-1,7)+row(2*n,7))/2/(scale/1000);
    end

    % putting the calculated X and Y corresponding to center of
dendrite
    % and its trunk diameter in proper place in result matrix
    result(n,2)=X;
    result(n,3)=Y;
    result(n,4)=TD;

end

% this loop calculates NNS, 3NNS and 6NNS based on calculated X and Y
of each dendrite
% it starts from the first point in the table and calculates the
distances from that point to all other points, then sorts
% the distances vector and select the first element as NNS, mean of
first
% three as 3NNS and mean of first six as 6NNS
for i=1:r/2
    z=1;
    for j=1:r/2
        if i~=j %
            distance(z)=sqrt((result(i,2)-(result(j,2)))^2+(result(i,3)-
(result(j,3)))^2);
            z=z+1;
        end
    end
    distance=sort(distance);
    NNS(i)=distance(1);
    NNS3(i)=mean(distance(1:3));
    NNS6(i)=mean(distance(1:6));

end

```

```

% converting spacings to micro meter
NNS=(NNS./(scale/1000))';
NNS3=(NNS3./(scale/1000))';
NNS6=(NNS6./(scale/1000))';

if (r/2)>= 15

    NNS_s=sort(NNS);
    top10_NNS_avg=mean(NNS_s(1:round((r/2)/10)));
    top10_NNS_std=std(NNS_s(1:round((r/2)/10)));
    bott10_NNS_avg=mean(NNS_s(length(NNS_s)-round((r/2)/10)+1:end));
    bott10_NNS_std=std(NNS_s(length(NNS_s)-round((r/2)/10)+1:end));

    TD=sort(result(:,4));
    top10_TD_avg=mean(TD(1:round((r/2)/10)));
    top10_TD_std=std(TD(1:round((r/2)/10)));
    bott10_TD_avg=mean(TD(length(TD)-round((r/2)/10)+1:end));
    bott10_TD_std=std(TD(length(TD)-round((r/2)/10)+1:end));

end

% calculating the mean and standard deviation on spacing for the whole
data
% set
NNS_Mean=mean(NNS);
NNS_STD=std(NNS);
NNS3_Mean=mean(NNS3);
NNS3_STD=std(NNS3);
NNS6_Mean=mean(NNS6);
NNS6_STD=std(NNS6);

% putting calculated spacings in the results table
result(:,5)=NNS;
result(:,6)=NNS3;
result(:,7)=NNS6;
result(:,1)=1:r/2; % filling the first column of result table with
dendrites numbers

% creating output excel file
filename = 'XY_TD_PDAS.xlsx';
A = {'Dendrite No.', 'Dendrite Center X', 'Dendrite Center Y', 'Dendrite
TD(um)', 'Dendrite NNS(um)', 'Dendrite 3 NNS(um)', 'Dendrite 6 NNS(um)'};
xlswrite(filename,A,1)
xlRange = 'E1';
xlswrite(filename,result,1,'A2')

if (r/2)>= 15
    B={'TD mean', 'TD std', 'NNS mean', 'NNS std', ...
        'Top 10% TD avg', 'Top 10% TD std', 'bottom 10% TD avg', 'bottom
10% TD std', ...
        'Top 10% NNS avg', 'Top 10% NNS std', 'bottom 10% NNS
avg', 'bottom 10% NNS std'};
    xlswrite(filename,B,1,'J3')

```

```

xlswrite(filename,[mean(result(:,4)),std(result(:,4)),mean(result(:,5))
, std(result(:,5))],...
        top10_TD_avg,top10_TD_std,bott10_TD_avg,bott10_TD_std...
top10_NNS_avg,top10_NNS_std,bott10_NNS_avg,bott10_NNS_std],1,'J4')

else
    B={'TD mean','TD std','NNS mean','NNS std'};
    xlswrite(filename,B,1,'J3')

xlswrite(filename,[mean(result(:,4)),std(result(:,4)),mean(result(:,5))
, std(result(:,5))],1,'J4')

end

```

## APPENDIX B

### TRUNK DIAMETER AND NEAREST NEIGHBOR SPACING MATLAB

#### CODE MODEL PREDICTION CALCULATIONS

```
clc;
[z zz]=size(data);
for i=1:z
    %%% Al 19Cu Properties
    % m=-3.3429; %K/wt%
    % Tm= 663.79+273.15; % K Linearized Pure Al Melting Point
    % TE= 548+273.15; % K
    % Tl=605.45+273.15;
    %
    % k=0.1203;
    % Dl=5388; % um^2/s
    % Gamma=0.1976; % K*um

    % %%% Al 7-Si Properties
    % m=-6.9468; %K/wt
    % Tm= 673+273.15; % K Linearized Pure Al Melting Point
    % TE= 577+273.15; % K
    % Tl=620+273.15; % K
    %
    % k=0.1273;
    % Dl=5409; % um^2/s
    % Gamma=0.1702; % K*um
    %
    % Co=7; % %
    % V=data(i,1); % um/s
    % Gl=data(i,2); % K/cm
    % Gm=data(i,3); % K/cm

    %%% Pb-6 Sb Properties
    m=-6.78; %K/wt
    Tm= 327.5+273.15; % K Linearized Pure Al Melting Point
    TE= 252.2+273.15; % K
    Tl=288.18+273.15; % K

    k=0.31;
    Dl=1130; % um^2/s
    Gamma=0.105; % K*um

    V=60; % um/s
    Co=data(i,1); % %
    Gl=data(i,2); % K/cm
    Gm=data(i,3); % K/cm
    %%%%%%%%%%%%%%%%%%%%%%%%%%%%%%%%%%%%%%%%%%%%%%%%%%%%%%%%%%%%%%%%%%%%%%%%%
    %%%%%%%%%%%%%%%%%%%%%%%%%%%%%%%%%%%%%%%%%%%%%%%%%%%%%%%%%%%%%%%%%%%%%%%%%

    Gl=Gl*100; %K/m
```

```

Gm=Gm*100; %K/m
V=V*10^-6; %m/s

Gamma=Gamma*10^-6; %K*m
Dl=Dl*10^-12; % m^2/s

delTo=m*Co*(k-1)/k;
V_=V*Gamma*k/(Dl*delTo);
G_=Gl*Gamma*k/(delTo)^2;

s=1-G_/V_;
%% Primary Dendrite Arm Spacing
a=-1.131-0.1555*log10(G_-)-0.7589e-2*(log10(G_-))^2;
lambda_=0.7798e-1*V_^(a-0.75)*(V_-G_)^0.75*G_^(-0.6028);

lambda=lambda_*Gamma*k/delTo;
lambda*2*10^6

%% Tip Undercooling

a=8.734+5.930*log10(k)+0.2578*(log10(k))^2;
b=0.4307-0.1656e-3*log10(k)-0.04455*(log10(k))^2;
c=1.454+0.2735*log10(G_-)+0.04145*(log10(G_-))^2+...
+0.001882*(log10(G_-))^3;
delT_s=(G_/V_)^c+a*V_^b+(1-a)*V_^(1.2*b);

delT_c=0.41*(V_-G_)^0.51;

delT_tip=(delT_s+delT_c)*delTo;

%% Tip Radius

R_tip=2*Gamma/(delT_c*delTo);
R_tip*10^6

%% Tip Composition in the solid

Ct=(delT_s*delTo+delTo/(1/k-1))/(-m/k);
% ((Tl-delT_tip-Tm)/m)*k

%% Trunk Diameter

Tf=(Tl-TE)-(Ct/k-Co)*(-m)
t=(Tf)/(Gm*V) % freezing time
to=22*R_tip/V;
TDo=6.59*R_tip;
TDo*10^6
TD=(96*Dl*Gamma/(V*Gm*(1-k))*log((1+V*Gm*t/(-m*Co))/(1+V*Gm*to/(-m*Co)))+TDo^3)^(1/3);
TD*10^6

```

```

% (delTo-delT_tip) / (Gm*V)
%
% Tt=Tl- (Dl*Gm/V);
% (Tt-TE) / (Gm*V)

Result(i,1)=s;
Result(i,2)=R_tip*10^6;
Result(i,3)=Ct;
Result(i,4)=lambda*2*10^6;
Result(i,5)=Tf;
Result(i,6)=t;
Result(i,7)=TD*10^6;
end

```

## APPENDIX C

### DETAILED PROCEDURE FOR FRACTION EUTECTIC DATA

#### EXTRACTION

1. Go to File – Open- Select the Image of the sample

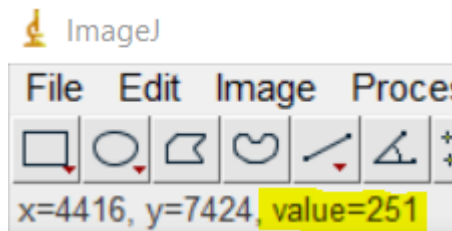
2. If image is not 8-bit already

a. Image- Type- 8-bit



3. Select the wand tool

a. Find the value of the higher white values in the sample by hovering mouse

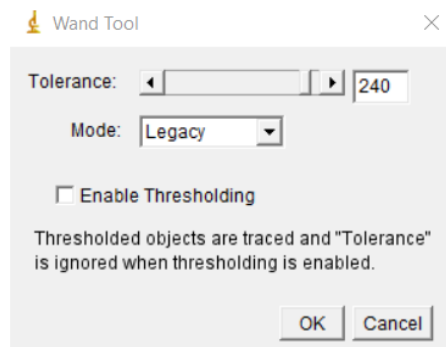


over that area and reading the value as shown below

b. Double click the wand tool and set your tolerance to some number slightly below this value

c. Click OK once tolerance is chosen

d. With the wand tool selected click within your sample and it should select



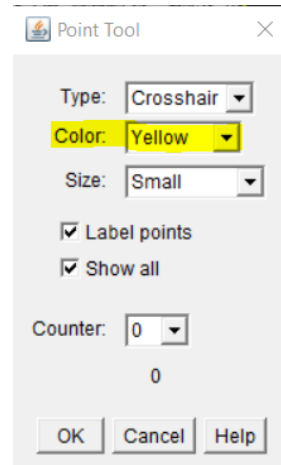
the perimeter of your sample

i. Note two different problems



1. If the color of wand tool is set to black you will be unable to see the selection

a. Double-click the point tool and change the color to

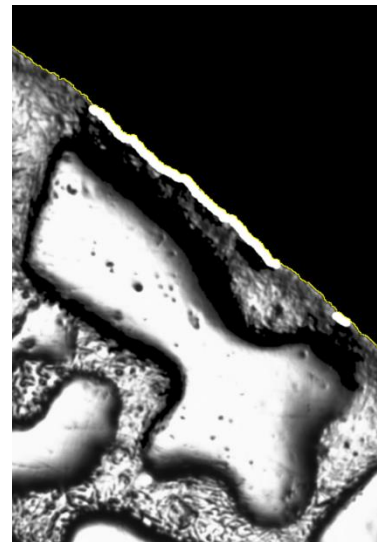
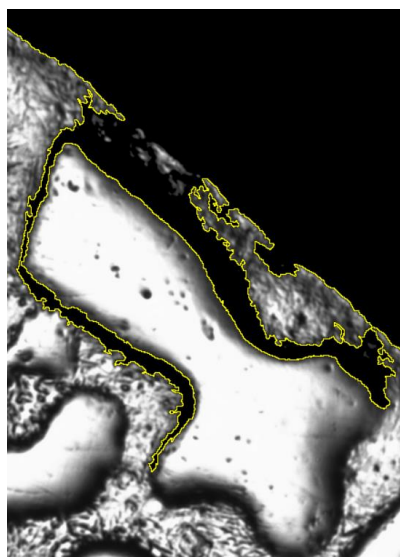


yellow if this problem is occurring


2. Another error is the Region selected by the wand tool could go into the sample some, which can be adjusted two ways

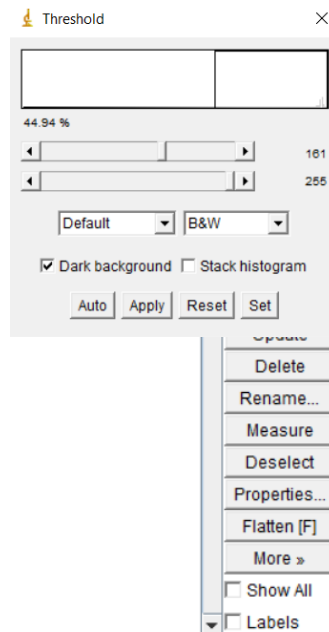
a. Lower the tolerance of the wand tool

3. Could also manually draw some of the perimeter lines with




the Paintbrush tool

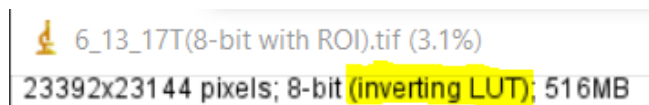
4. With your sample region selected go to Analyze- Tools- ROI Manager
5. Click Add [t] which adds this selection to the ROI Manager
6. Deselect this region by selecting the Rectangle Tool  and clicking anywhere on the picture file
7. Image- Adjust- Threshold



8. Use the default method and click apply
  - a. Can be manually adjusted due to quality of the image (primarily shadowing)
 

by selecting the color of the dendrites (with the color picker tool ) and manually filling them in with the brush tool

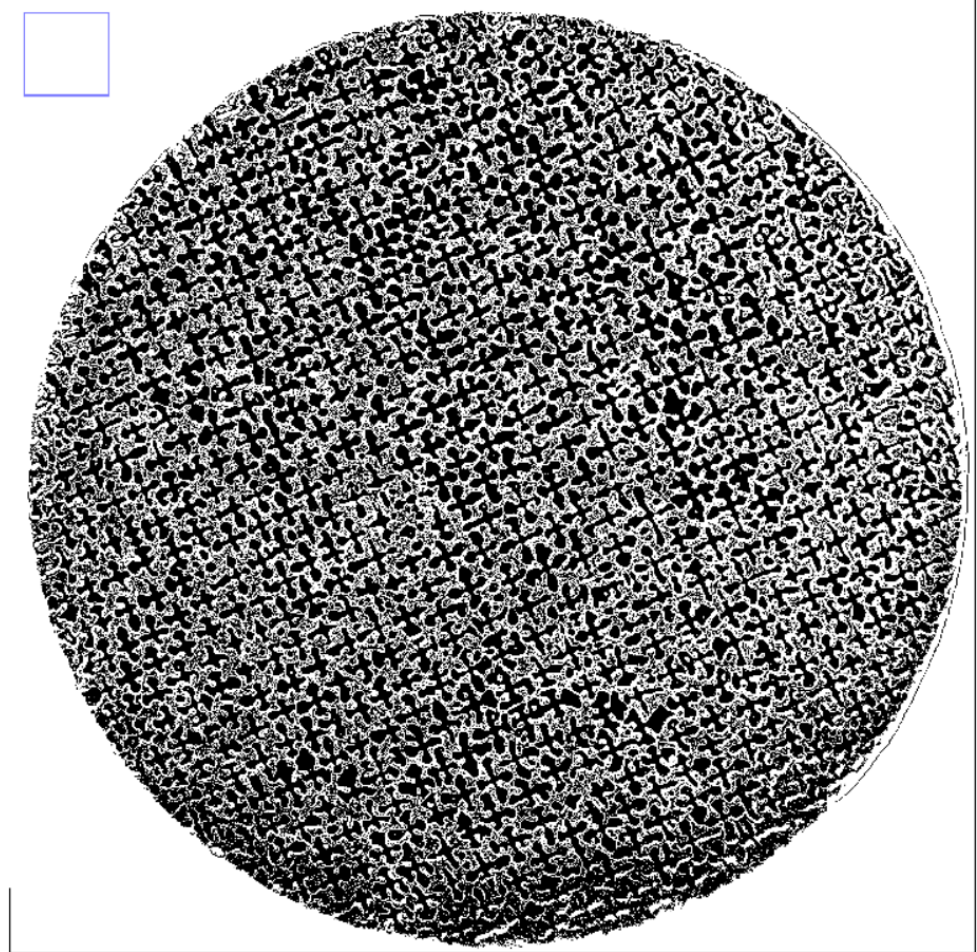
9. Next step is to remove the inverting LUT



- a. Image- Lookup Tables- Invert LUT
- b. Edit- Invert

- i. This makes alpha phase black and have a value of zero and image

23392x23144 pixels; 8-bit; 516MB



should look like this

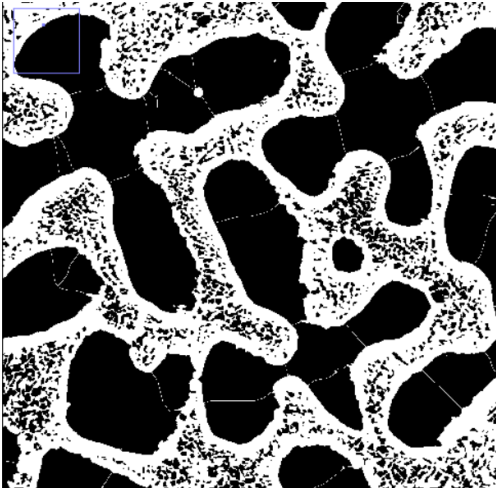
10. Next remove the scale in the bottom right corner if there is one

- a. Rectangle tool the region with scale and fill with white

11. Important to now save image as a different file than the original image

- a. File- Save as- .tiff

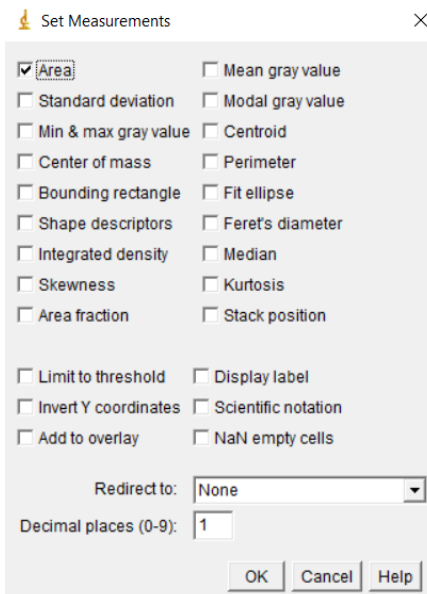
## 12. Process- Binary- Watershed



- a. This separates the primary alpha phase from the alpha phase in the eutectic

## 13. Now you need to get rid of the alpha phase in the eutectic region

- a. Find a large particle in eutectic region
- b. Select the wand tool with a threshold of 1
- c. Select that particle
- d. Analyze- Set Measurement- Area

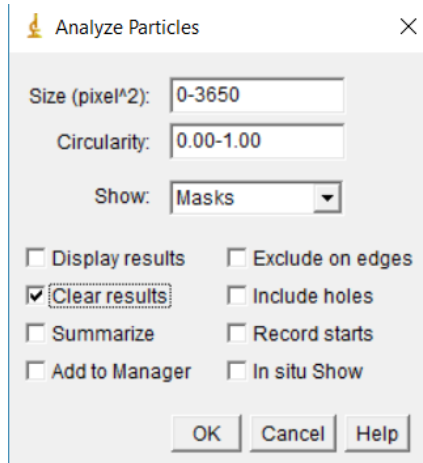


- e. Analyze Measure (control M)
- f. Deselect that particle to make sure you have entire picture in selection

g. Analyze- Analyze Particles

i. Size: 0-“Number slightly higher than area of the particle selected”

ii. Show: Masks



h. Click OK

14. New Image will open

15. Edit- Selection- Create Selection

a. Add to ROI Manager

b. Close the newly created window

16. Click on the ROI you just created to selected it

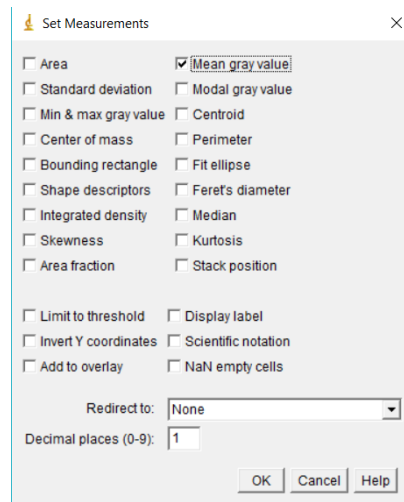
a. Select white with the color picker tool

b. Edit- Fill

i. Or control F

17. Select original ROI (boundary of your sample)

## 18. Analyze-Set Measurements- Mean Gray Value



a. Analyze- Measure

i. Or control M

19. Divide the number you get by 255 to get fraction eutectic

20. These next steps are not always necessary but can help get a better fraction eutectic

21. Process-Binary- Dilate

22. Process- Binary- Erode

23. Measure the Mean gray value and divide by 255 to get fraction eutectic

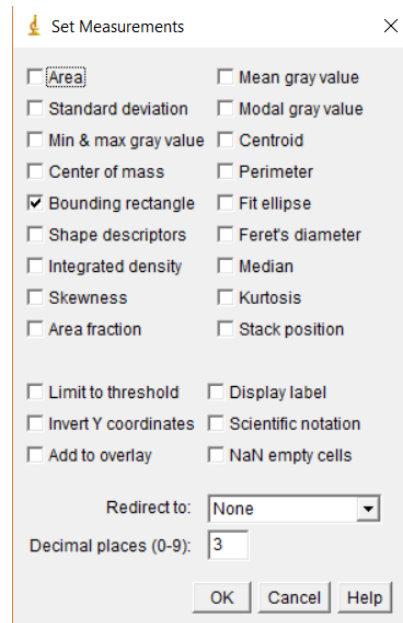
a. The reason you typically don't need this step is because the value difference is so small as seen below


Results	
	Mean
1	150.1
2	149.4

## APPENDIX D

### DETAILED PROCEDURE FOR NEAREST NEIGHBOR SPACING AND TRUNK DIAMETER DATA EXTRACTION

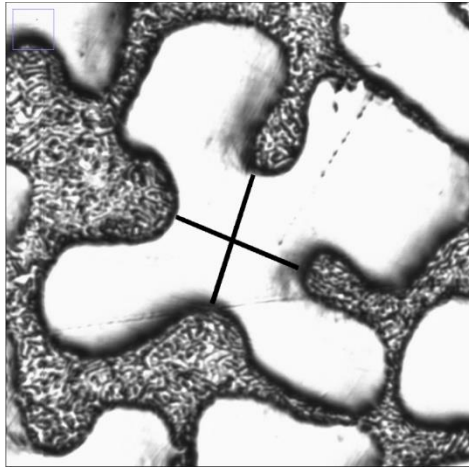
1. Open Program ImageJ
2. File-Open-Select Image of sample
3. Analyze-Set Measurements-Bounding rectangle



4. Double click color picker tool  - Select black
5. Double click straight tool  and make line width approximately 10



6. Make X's on the dendrites to get the enter and trunk diameter



7. Control F is fill line and control M is measure
8. Copy all the line data from ImageJ into Excel and save
9. Open program MATLAB
10. Run MATLAB script XY\_TD\_NNS\_MST
  - a. Note all items need to be in same folder for MATLAB to run Correctly
  - b. Make sure the Scale at the top of the Script is set to what is the appropriate conversion between pixels and millimeters based on the image taken (default is for 50 times magnification)
    - i. This can be done by measuring how many pixels your scale in ImageJ is with the straight line tool

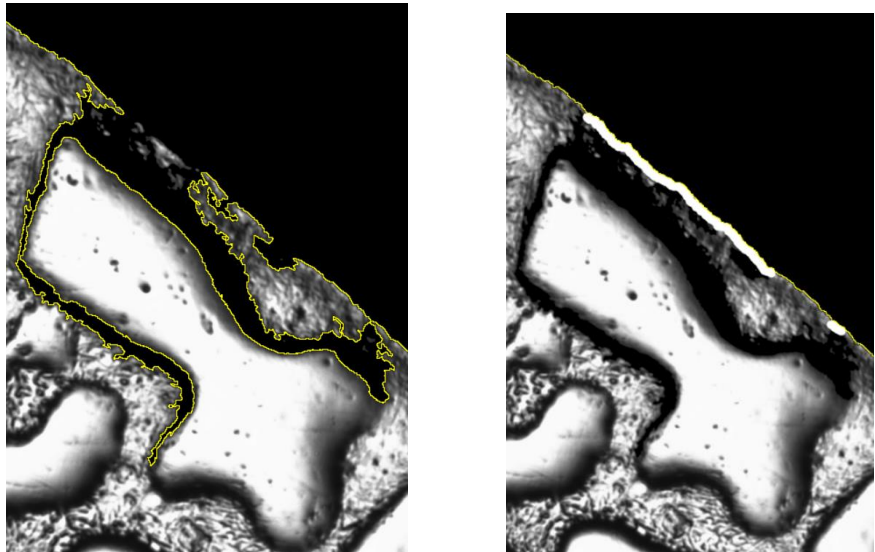
```
5 - scale=2420; % number of pixels per mm in original image
```

- c. When Prompted to select file select the Excel File you just saved
- d. Will need the area of the Region of Interest in pixels
  - i. This is obtained through ImageJ using the Wand Tracing Tool
    1. If background is black set tool to have a tolerance of around 240
      - a. Adjust this to get best fit around the edge of the sample





2. If any of the Region of interest isn't selected you can manually add back in parts by using the Paintbrush tool



- e. Figure 1 is the Minimum Spanning Tree and Figure 2 is just the center of the dendrites
- f. All the calculations are automatically saved to an Excel file in the same folder called XY\_TD\_PDAS
  - i. Note the data Row 4 Column J and beyond is in Micrometers

## APPENDIX E

Table IX COMPLETE SUMMARY OF RESULTS FOR PB-SB-12-24

Sample ID	Location	Number of Dendrites	Area	f_e	C_s	f_s	TD_Avg	TD_STD	NNS_Avg	NNS_STD	Gm	Gl	NNS_HL	Delta_T	Freez_Time	TD_Pred
UNITS	cm		mm <sup>2</sup>		wt%		μm	μm	μm	μm	K/cm	K/cm	μm		s	μm
Pb-Sb-12-24-14-1	1		67.89	0.28	4.32											
Pb-Sb-12-24-14-2	2		70.64	0.31	4.64											
Pb-Sb-12-24-14-3	3	223	70.90	0.33	4.90	0.04	140.24	8.73	399.42	77.03	10.50	11.25	568	34.05	3130	100.07
Pb-Sb-12-24-14-4	4		70.65	0.34	5.04	0.09					10.65	11.50	566	34.01	3083	98.87
Pb-Sb-12-24-14-5	5	301	70.90	0.37	5.28	0.13	129.78	8.05	355.11	68.27	10.80	11.75	567	33.96	3035	97.23
Pb-Sb-12-24-14-6	6		70.28	0.36	5.24	0.18					10.80	12.00	561	33.96	3035	97.42
Pb-Sb-12-24-14-7	7	258	71.45	0.34	4.99	0.22	129.81	8.47	366.32	74.00	10.80	12.25	549	34.01	3040	98.67
Pb-Sb-12-24-14-8	8		69.10	0.34	4.96	0.27					10.80	12.50	544	34.02	3040	98.81
Pb-Sb-12-24-14-9	9		70.60	0.34	5.05	0.31					11.45	12.75	541	34.00	2866	96.51
Pb-Sb-12-24-14-10	10	347	70.40	0.35	5.08	0.36	129.94	8.82	341.27	58.49	12.10	13.00	537	33.98	2711	94.61
Pb-Sb-12-24-14-11	11		70.29	0.35	5.11	0.40					12.10	13.25	534	33.97	2710	94.45
Pb-Sb-12-24-14-12	12		70.15	0.34	4.98	0.44					12.20	13.50	526	34.00	2690	94.82
Pb-Sb-12-24-14-13	13	471	70.02	0.33	4.85	0.49	128.72	9.11	320.55	43.91	12.10	13.80	518	34.02	2714	95.71
Pb-Sb-12-24-14-14	14	455	69.80	0.34	5.01	0.53	125.91	7.91	321.67	43.82	12.95	14.70	508	33.97	2532	92.82
Pb-Sb-12-24-14-15	15		70.03	0.34	5.04	0.58					13.80	15.60	496	33.95	2375	90.75
Pb-Sb-12-24-14-16	16	458	70.53	0.34	4.99	0.62	124.34	8.35	318.87	45.51	13.80	16.50	483	33.95	2375	90.99
Pb-Sb-12-24-14-17	17		70.77	0.35	5.10	0.67					13.80	17.40	474	33.92	2372	90.46
Pb-Sb-12-24-14-18	18		70.17	0.35	5.15	0.71					13.80	18.30	465	33.89	2371	90.23
Pb-Sb-12-24-14-19	19	530	70.34	0.36	5.18	0.76	118.60	8.24	299.14	40.01	14.00	19.20	456	33.87	2335	89.65
Pb-Sb-12-24-14-20	20		69.62	0.38	5.41	0.80					14.65	20.10	452	33.81	2228	87.31
Pb-Sb-12-24-14-21	21		70.30	0.39	5.57	0.84					15.50	21.00	446	33.77	2103	85.07
Pb-Sb-12-24-14-22	22	510	70.15	0.40	5.65	0.89	107.33	8.44	299.02	47.45	15.50	21.90	440	33.73	2101	84.72
Pb-Sb-12-24-14-23	23		70.04	0.44	6.07	0.93					16.35	22.80	439	33.64	1986	81.69
Pb-Sb-12-24-14-24	24	514	69.87	0.46	6.28	0.98	94.08	68	288.41	48.87	16.35	23.70	435	33.58	1983	80.93

Table X COMPLETE SUMMARY OF RESULTS FOR PB-SB-12-22

Sample ID	Location	Number of Dendrites	Area (mm <sup>2</sup> )	f <sub>e</sub>	C <sub>s</sub>	f <sub>s</sub>	TD _Avg	TD _STD	NNS _Avg	NNS _STD	Gm	Gl	NNS _HL	Delta _T	Freez _Time	TD _Pred
UNITS	cm		mm <sup>2</sup>		wt%		μm	μm	μm	μm	K/cm	K/cm	μm		s	μm
Pb-Sb-12-22-14-1	1		69.84	0.36	5.19											
Pb-Sb-12-22-14-2	2		69.26	0.20	3.40											
Pb-Sb-12-22-14-3	3	489	70.24	0.34	5.04	0.04	88.94	6.21	257.79	55.96	8.30	9.20	319	32.53	621	59.10
Pb-Sb-12-22-14-4	4		69.85	0.38	5.41	0.09					8.30	9.20	326	32.37	618	58.00
Pb-Sb-12-22-14-5	5	362	69.93	0.36	5.22	0.13	85.60	8.20	269.15	89.40	8.30	9.20	322	32.45	620	58.55
Pb-Sb-12-22-14-6	6		69.80	0.38	5.44	0.18					8.30	9.20	326	32.36	618	57.91
Pb-Sb-12-22-14-7	7	420	69.72	0.39	5.53	0.22	79.59	7.14	255.75	68.82	8.30	9.20	328	32.32	617	57.65
Pb-Sb-12-22-14-8	8		69.65	0.38	5.44	0.27					8.30	9.20	326	32.36	618	57.91
Pb-Sb-12-22-14-9	9	456	69.70	0.39	5.57	0.31	77.55	6.73	243.45	68.46	8.60	9.70	321	32.30	595	56.87
Pb-Sb-12-22-14-10	10	399	69.73	0.34	5.04	0.36	81.72	8.32	256.21	80.69	9.00	10.10	305	32.52	573	57.53
Pb-Sb-12-22-14-11	11		69.88	0.36	5.17	0.40					9.35	10.60	301	32.47	550	56.43
Pb-Sb-12-22-14-12	12	478	69.53	0.37	5.37	0.44	78.42	7.74	246.65	79.70	9.70	11.00	299	32.38	529	55.18
Pb-Sb-12-22-14-13	13		74.14	0.39	5.53	0.49					10.10	11.50	295	32.31	507	54.02
Pb-Sb-12-22-14-14	14	561	73.23	0.39	5.59	0.53	74.19	6.25	229.01	59.39	10.50	11.90	292	32.29	487	53.18
Pb-Sb-12-22-14-15	15		72.59	0.39	5.55	0.58					11.10	12.40	286	32.30	461	52.30
Pb-Sb-12-22-14-16	16	771	72.32	0.38	5.45	0.62	70.55	4.63	216.28	59.90	11.80	12.80	280	32.35	434	51.51
Pb-Sb-12-22-14-17	17		70.82	0.39	5.51	0.67					12.10	13.30	276	32.32	423	50.93
Pb-Sb-12-22-14-18	18	922	70.61	0.40	5.65	0.71	69.06	3.78	205.30	42.67	12.10	13.80	273	32.26	423	50.59
Pb-Sb-12-22-14-19	19		70.06	0.40	5.70	0.76					12.80	14.60	267	32.24	399	49.53
Pb-Sb-12-22-14-20	20	918	70.36	0.41	5.76	0.80	62.61	3.75	202.68	44.84	13.70	15.40	261	32.21	373	48.29
Pb-Sb-12-22-14-21	21		69.94	0.41	5.78	0.84					14.50	16.20	255	32.20	352	47.34
Pb-Sb-12-22-14-22	22	932	68.89	0.48	6.49	0.89	58.93	3.29	196.74	45.77	15.30	17.00	258	31.92	331	45.03
Pb-Sb-12-22-14-23	23		69.21	0.48	6.51	0.93					16.00	17.60	254	31.91	316	44.35
Pb-Sb-12-22-14-24	24	869	67.31	0.59	7.60	0.98	45.53	3.71	193.35	44.63	16.70	18.40	261	31.51	299	41.83

Table XI COMPLETE SUMMARY OF RESULTS FOR PB-SB-3

Sample ID	Location (cm)	Number of Dendrites	Area (mm^2)	f_e	C_s	TD_Avg	TD_STD	NNS_Avg	NNS_STD	Gm	Gl	NNS_HL	Delta_T	Freez_Time	TD_Pred
UNITS	cm		mm <sup>2</sup>		wt%	μm	μm	μm	μm	K/cm	K/cm	μm		s	μm
Pb-Sb-3-16	-83.00	648	123.54	0.31	4.84	140.70	11.15	344.58	48.38	12.56	10.01	506	34.11	2963	101.09
Pb-Sb-3-14	-60.00	676	122.59	0.36	5.50	132.07	12.16	343.38	53.27	12.55	10.29	522	33.97	2870	97.00
Pb-Sb-3-10	-29.00	735	125.22	0.40	5.92	119.69	9.78	336.79	52.91	12.54	10.67	532	33.88	2761	94.04
Pb-Sb-3-8	-17.50	723	124.27	0.33	5.16	126.69	9.71	333.37	51.14	12.53	10.81	515	34.04	2738	97.00
Pb-Sb-3-6	-9.00	843	125.82	0.36	5.50	126.40	11.61	304.49	48.89	12.57	10.94	522	33.97	2700	95.06
Pb-Sb-3-5	-3.50	876	125.62	0.31	4.90	126.28	12.58	299.50	46.02	12.79	11.18	504	34.09	2651	97.18
Pb-Sb-3-32	-0.81	380		0.38	5.74	145.78	20.33	306.55	48.31	12.90	11.30	521	33.91	2610	93.02
Pb-Sb-3-33	-0.45	174		0.52	7.26	147.38	15.94	317.43	70.17	12.92	11.32	553	33.62	2583	87.35
Pb-Sb-3-34	0.25	119		0.27	4.45	143.44	14.27	304.87	49.25	12.95	11.35	490	34.19	2619	99.02
Pb-Sb-3-35	1.00	107		0.28	4.54	135.90	10.76	315.71	58.31	12.98	11.38	492	34.17	2611	98.45
Pb-Sb-3-36	2.02	123		0.29	4.62	133.33	8.02	297.84	58.26	13.02	11.43	493	34.15	2598	97.89
Pb-Sb-3-37	3.09	99		0.49	7.00	121.31	12.39	308.17	50.80	13.06	11.47	545	33.67	2553	87.83
Pb-Sb-3-4	3.50	184	30.44	0.36	5.54	114.83	8.80	296.96	52.24	13.08	11.49	514	33.95	2570	93.36
Pb-Sb-3-3	8.00	183	30.57	0.29	4.63	122.49	7.31	291.52	74.77	13.26	11.69	490	34.14	2540	97.11
Pb-Sb-3-2	12.00	206	30.31	0.31	4.87	120.59	8.77	281.92	55.74	13.43	11.86	493	34.09	2499	95.45
Pb-Sb-3-1	15.00	204	30.80	0.33	5.10	119.80	8.01	281.51	46.04	13.55	12.00	496	34.04	2466	93.98
Pb-Sb-3-20	28.37	126	20.08	0.37	5.62	117.87	7.23	293.88	51.68	14.09	12.58	499	33.92	2345	90.27
Pb-Sb-3-22	39.87	130	23.62	0.41	6.10	108.94	6.78	321.97	56.36	14.63	13.16	500	33.82	2235	87.06
Pb-Sb-3-25	66.87	160	26.50	0.42	6.17	105.51	7.02	313.64	62.98	16.71	15.43	473	33.78	1904	82.36
Pb-Sb-3-27	89.87	192	29.40	0.49	6.92	94.78	7.47	310.16	56.05	18.49	17.37	466	33.61	1683	76.81
Pb-Sb-3-30	133.87	175	30.33	0.51	7.12	79.09	5.17	305.12	64.78	21.88	21.08	435	33.53	1383	71.50
Pb-Sb-3-31	148.87	123	29.26	0.53	7.41	80.95	6.97	315.05	88.73	23.03	22.35	430	33.47	1302	69.38

Table XII COMPLETE SUMMARY OF RESULTS FOR PB-SB-1

Sample ID	Location (cm)	Number of Dendrites	Area (mm <sup>2</sup> )	f_e	C_s	TD_Avg	TD_STD	NNS_Avg	NNS_STD	Gm	Gl	NNS_HL	Delta_T	Freez_Time	TD_Pred
UNITS	cm		mm <sup>2</sup>		wt%	μm	μm	μm	μm	K/cm	K/cm	μm		s	μm
Pb-Sb-1-20	-93.00	130	29.93	0.24	4.61	158.29	11.34	359.67	50.13	10.93	11.06	586	34.30	3607	109.26
Pb-Sb-1-19	-73.00	170	30.27	0.23	4.55	158.31	13.70	321.49	54.20	12.44	12.92	547	34.28	3167	105.03
Pb-Sb-1-18	-53.00	199	32.38	0.20	4.03	152.53	10.87	314.93	48.31	13.95	14.78	504	34.35	2830	104.16
Pb-Sb-1-17	-43.00	205	30.87	0.21	4.19	149.47	10.73	297.34	39.10	14.71	15.71	495	34.30	2680	101.41
Pb-Sb-1-16A	-33.00	198	30.22	0.22	4.35	145.56	11.74	304.09	43.45	15.46	16.64	487	34.25	2547	98.86
Pb-Sb-1-1	-28.00	206	30.35	0.17	3.61	150.46	11.42	302.54	48.60	15.84	17.10	465	34.40	2496	102.54
Pb-Sb-1-4	-16.80	222	30.39	0.22	4.40	148.09	9.97	292.28	42.61	16.69	18.14	471	34.22	2357	96.14
Pb-Sb-1-6	-9.60	220	30.11	0.23	4.49	143.64	10.49	289.98	50.54	17.21	18.83	466	34.19	2283	94.70
Pb-Sb-1-7	-6.40	223	30.00	0.21	4.20	143.08	10.12	285.04	40.24	17.32	19.22	456	34.24	2272	96.06
Pb-Sb-1-8	-3.30	218	30.03	0.26	4.89	142.48	8.06	283.63	45.17	17.42	19.60	466	34.10	2250	92.34
Pb-Sb-1-9	-0.70	204	30.00	0.25	4.75	142.45	9.64	292.19	46.81	17.51	19.92	461	34.12	2240	92.86
Pb-Sb-1-11	4.40	1159	125.90	0.28	5.13	145.49	14.98	260.87	42.36	17.68	20.55	462	34.04	2213	90.79
Pb-Sb-1-12	7.40	1137	126.31	0.26	4.93	152.49	14.59	270.84	36.34	17.78	20.92	455	34.07	2202	91.53
Pb-Sb-1-13	10.40	1056	126.11	0.27	5.05	145.39	13.37	277.46	38.08	17.88	21.29	454	34.04	2188	90.81
Pb-Sb-1-14	14.10	1027	126.50	0.23	4.51	149.63	16.07	275.34	40.61	18.00	21.74	440	34.13	2180	93.20
Pb-Sb-1-15	19.20	1177	127.17	0.20	4.10	153.97	16.69	269.23	39.76	18.17	22.37	427	34.20	2164	95.09
Pb-Sb-1-16	26.80	1303	128.76	0.24	4.67	147.63	15.40	266.20	38.87	18.43	23.30	431	34.08	2125	91.67
Pb-Sb-1-2	37.00	1303	126.11	0.26	4.91	141.04	13.19	262.06	40.34	18.77	24.56	425	34.01	2083	89.98
Pb-Sb-1-22	52.00	1097	126.68	0.28	5.19	124.66	10.93	280.16	40.73	20.59	23.93	435	33.97	1896	86.10
Pb-Sb-1-23	67.00	1073	126.76	0.30	5.49	118.15	10.59	279.94	42.06	22.50	23.12	446	33.93	1733	82.46
Pb-Sb-1-24	82.00	1166	126.43	0.39	6.67	107.52	8.05	274.02	43.90	24.41	22.31	471	33.74	1589	76.29

Where the following labels signify:

f <sub>e</sub>	fraction eutectic
C <sub>s</sub>	average concentration
TD_Avg	average trunk diameter
TD_STD	standard deviation for measured trunk diameter values
NNS_Avg	average nearest neighbor spacing
NNS_STD	standard deviation for measured nearest neighbor spacing
G <sub>m</sub>	mushy zone thermal gradient
G <sub>l</sub>	thermal gradient near the tip
NNS_HL	Hunt-Lu <sup>18</sup> predicted nearest neighbor spacing values
Delta_T	undercooling near the tip
Freeze_Time	time it takes to freeze leading fluid near the tip
TD_Pred	Tewari et. al predicted trunk diameter values